Department of Physics

Final year project

Observations with the Bristol Optical Telescope

Author:
Richard D Painter
Degree:
Physics w/ Astrophysics BSc (F3F5)

Supervisors:
Dr. Ben Maughan
Dr. Rhys Morris
Assessor:
Dr. Henkjan Gersen

Project number:
A6
Word count:
11,720

July 14, 2011

H H Wills Physics Laboratory, University of Bristol, Tyndall Avenue, Bristol, BS8 1TL

DECLARATION

Manual data collection and calibration data analysis was conducted equally between both project students. Empirical data from each observing session was analyzed individually by each student, although collaboration was frequent and students often applied a similar methodology throughout this stage of the data analysis. For the duration of the project period, weekly meetings were held between project students and supervisors where feedback on students' results and experimental technique was given. This often prompted students to discuss and devise new methods to obtain and analyze their data. Students were given access to previous project students' formal reports and data, which was of use during the early data calibration stages. Unix and IDL training was provided to both students and sample IDL code was provided to enable students to grasp the basics of the programming language. Unless otherwise stated, all IDL code used to generate the data presented in this report was written by the project students themselves, from scratch.

ACKNOWLEDGEMENTS

Significant credit should be given to the project supervisors; Drs Maughan and Morris voluntarily gave up considerable amounts of their time to meet with project students each week and regularly provided insightful feedback and innovative ideas to drive the project forwards. Credit is owed to the previous project students; James Flynn, Matthew Golding and Paul Huyton for providing past reports and data which the project students were able to work from. Thank you to postgraduate students Paul Giles and Alex Lockey for remaining in the H.H. Wills Physics Laboratory building after hours during term-time to enable the project students to obtain empirical astronomical data on 07 March 2011 and 24 March 2011.

The calibration and data analysis of the Coldrick Observatory SBIG ST-7E CCD - Meade 10$''$ LX200 setup is presented. At -5°C the CCD device responds linearly to dark current and photons up to 40,000 ADU and is susceptible to ambient light leakage. $\sim$ 10% of pixels in the CCD array are found to be hot pixels, $\sim$ 30% warm pixels and $\sim$ 10% cool pixels. The zero-point calibration factor for accurate r$'_{mag}$ calibration is 3.03$\pm$ 0.16 not correcting for extinction; 2.56 $\pm$ 0.01 at zero airmass. The lowest observable magnitude with through r$'$ filter is 0.87 $\pm$ 0.01 V$_{mag}$. Bristol seeing conditions do not correlate strongly with altitude or azimuth. 0.27 $''$ resolution is able to be achieved in 6.50 $\pm$ 0.24 $''$ seeing. Bad seeing values decrease the Coldrick LX-200 resolution capabilities. The setup may be tentatively sensitive to variable star magnitude fluctuations, however further investigation is required.

1 INTRODUCTION

The Coldrick Observatory (2.6020E, 51.4589N, 80 m) situated on the roof of the H.H Wills Physics Laboratory was commissioned and funded by Mr. William P. Coldrick, a University of Bristol alumnus. The primary instrument situated in the observatory is a Weston Antennas 6 metre Cassegrain radio telescope, however an observing dome also exists housing a 10” Schmidt-Cassegrain Catadioptric (f/10) Meade LX200 optical telescope, with accompanying Santa Barbara Instrument Group ST-7E CCD imager [1].

For over a decade since its inception, the Meade optical telescope has not been used for research purposes. Dr Maughan of the University of Bristol Astrophysics Group oversees the operation of this telescope and in 2009/10 supervised the first undergraduate BSc project using the telescope, reinstating its use as a scientific tool. The 2009/10 project aimed to calibrate the CCD and telescope devices, in order determine the quality and reliability of empirical data which could be obtained [2] [3] [4].

Using the previous project as a stepping stone, the 2010/11 undergraduate project hopes to continue with the pioneering work performed by the previous project students. The project aims to perform accurate calibration with the CCD imager, enabling sufficient data reduction to take place on empirical astronomical data. The ability to measure and calibrate r$'$ magnitudes of stellar sources will be investigated using the Meade LX-200 device and the observing conditions in the Bristol area will be quantified. The ability to image double star sources down to arcsecond resolutions and the sensitivity towards variable star magnitude fluctuations shall also be investigated using the Coldrick Observatory optical setup.

2 DETAILED BACKGROUND

2.1 TELESCOPE CHARACTERISTICS

Telescopes are designed as scientific tools to enable observers on Earth to resolve objects in the sky which they are not able to do so with their own eyes. The performance of any given telescope is able to be characterized, and this characterization determines the physical properties of the telescope. Different telescopic characteristics are required by astronomers, depending of the types of observation they intend to make. Choosing the correct type of telescope with the correct characteristics is therefore an important decision process for an astronomer to make.

The main characteristics of astronomical telescopes shall be briefly discussed, culminating with a discussion of the Schmidt-Cassegrain telescope set up used in this investigation.

2.1.1 LIGHT-GATHERING POWER

Telescopes enable faint objects in the night sky to be observed, which are not usually visible to the naked human eye. A quantifiable characteristic of a telescope is its light-gathering power, defined as

$$\textit{light-gathering power} = (D_0/D_i)^2 \tag{1}$$

where D$_0$ is the diameter of the objective mirror and D$_i$ is the diameter of the instrumental aperture used to collect the light, assuming all light which is reflected off the objective mirror passes through this aperture. For this investigation, D$_i$ corresponds to the nose-piece of the ST-7E CCD camera used, which was 1.5$''$ in diameter [5] [7].

It can therefore by shown that for a larger objective mirror diameter and/or smaller instrumental aperture, the light-gathering power of a telescope can be improved.

The light gathering power for the setup in this investigation has been calculated as 47.84, using a value of 10.375$''$ for D$_0$ [1].

2.1.2 FIELD-OF-VIEW

A telescope, though free to move in 360° is only able to observe a quantifiable area of the night sky at any given time. A crude analogy is that of a picture frame: if you were to look up at the sky with an empty picture frame held in front of you, you would only be able to observe the area of the sky inside of the frame at any given time (Fig. 2). Astronomers characterize the angular area inside of the ‘frame’ as the field-of-view of the telescope.

Angular area is measured in units of arcminutes $'$ ($\frac{1}{60}$th $^\circ$) and arcseconds $''$ ($\frac{1}{60^2}$th $^\circ$ or $\frac{1}{60}$th $'$).

The angular field-of-view in radians along a particular dimension (vertical or horizontal), θ is proportional to the linear size of the detector used to collect the data, l and inversely proportional to the focal length of the system, f_0 as

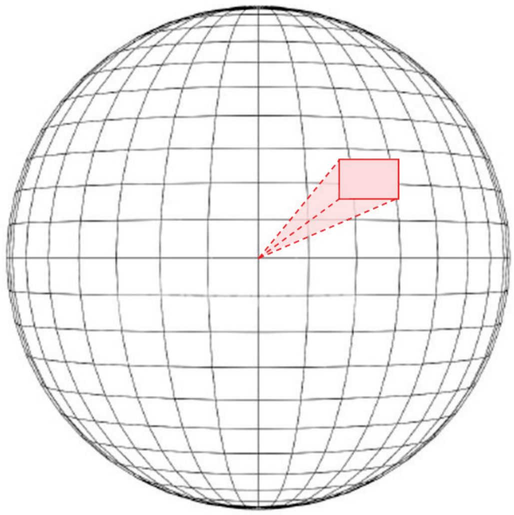

FIG. 1. An analogy of the field-of-view concept. An observer is standing at the centre of the celestial sphere and looking outwards. The angular field-of-view can be measured along any dimension of the rectangle: vertically, horizontally or diagonally. The field-of-view remains constant, no matter where the rectangle moves on the sky.

$$\theta = l/f_0 \tag{2}$$

Increasing the dimensions of a telescope detector or decreasing the focal length of its objective mirror therefore increases the angular field-of-view which is able to be observed by the telescope.

The Meade 10″ LX-200 Schmidt-Cassegrain telescope has a f-number of *f/10*. The f-number, also referred to as the "speed" of an optical system is defined as the focal length divided by the aperture diameter. The focal length of the device is therefore 2500mm (100″) [1].

The angular field-of-view of the Meade LX-200 Schmidt-Cassegrain telescope with SBIG ST-7E CCD camera attachment has been found to be 9.49 ′ x 6.32 ′, for 6.9 x 4.6mm KAF0401E CCD dimensions [8].

2.1.3 IMAGE SCALE

The image scale, I is a measure of how well a telescope is able to magnify astronomical objects, i.e. how 'far' it is able to see into space. Astronomers quote this figure in arcsec mm^{-1}, or how many arcseconds of the sky are represented by 1 mm in the imaging device. I is inversely proportional to the effective focal length of the system, f_0 as

$$I\,/arcsec\;mm^{-1} = \frac{1}{(f_0/mm)\ \mathrm{x}\ tan(')} \tag{3}$$

As both field of view and image scale are inversely proportional to f_0, they are both proportional to each other. Therefore, if the field of view of a system is decreased, the image scale will also decrease seeing as there is less angular distance represented by each pixel [5].

The image scale for the setup in this investigation can be calculated as 0.74″ pixel^{-1} for a 765x510 array of pixels with dimensions 9x9μm.

2.1.4 ANGULAR RESOLUTION

Distant astronomical objects are assumed to be point-like sources. Parallel rays from a point-like object will not, however appear as a point when viewed through a telescope due to diffraction of the light by the telescope aperture. The extent of diffraction decreases with an increase in aperture size, yet is still intrinsically present in any telescope design. Instead of a point, an extended image of the source will be visible as a point spread function or Airy disk (Fig. 2ia) [5].

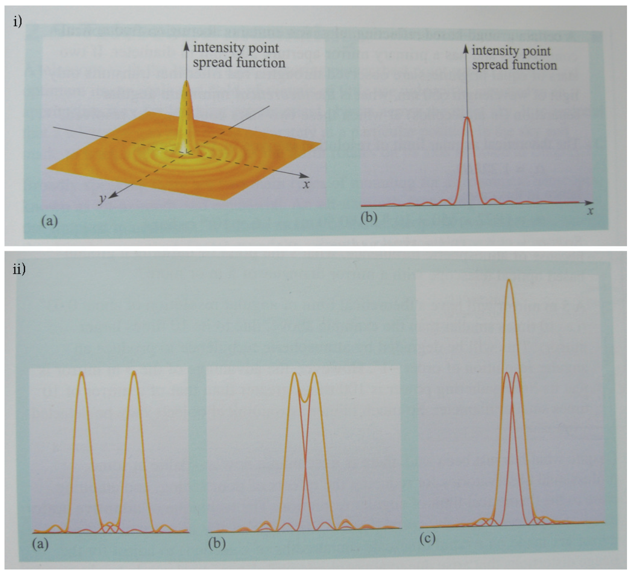

FIG. 2. *ia*: Point spread function from a point source after passing through a circular aperture. Successive maxima and minima are formed due to diffraction of the incident light. *ib* Point spread function intensity and spread function. The FWHM of the central peak dictates the "seeing" of the astronomical object. *iia* Two sources resolved. *iib* Two sources are just resolved when the maximum of one point spread function lies above the first minimum of an adjacent PSF function: the Rayleigh criterion. *iic* Two sources unresolved, as their maxima peaks are closer than α_c [5].

The point spread function of an object will vary due to atmospheric affects such as turbulence and due to optical effects such as aberrations. In either case, such effects will cause the point spread function curve to broaden. Astronomers quantify the quality of observing on a given night by a quantity known as "seeing". Seeing is defined as the full width at half maximum (FWHM) of the point spread function peak measured for a given object.

The lower the value of the seeing, the better the observing conditions on the night. For example, on a turbulent day the

PSF function will broaden causing a larger seeing value to occur. The seeing in the Bristol area is one of the factors that shall be quantified during this investigation.

Assuming perfect weather conditions and no aberrations in the optical setup, a telescope is said to be diffraction-limited. At this point, the point spread function peak width will be at a minimum value. In these conditions it is able to define the angular resolution of a telescope - the minimum separation possible between two equally bright sources for the telescope to resolve them as two separate sources. Astronomical convention states that for two such objects to be resolved, the peak of the PSF from one object must fall on the first minimum in the PSF function of the second object (Fig. ref).

The Rayleigh criterion determines the angular resolution limit, α_c in radians when two objects are just able to be resolved, as depicted in Fig. 2iib, as

$$\alpha_c = 1.22\lambda/D \tag{4}$$

Where λ is the wavelength of incident light and D is the diameter of the telescope aperture. The theoretical resolution limit of the Meade LX-200 10$''$ telescope, assuming λ = 626nm in the r$'$ waveband is 0.62 $''$. This theoretical limit will be investigated on empirical data obtained during this investigation.

2.2 SCHMIDT-CASSEGRAIN TELESCOPE

The telescope setup used in this investigation is of a Schmidt-Cassegrain design. This design shall be discussed in detail, including characteristics which make it a suitable telescope architecture for this investigation.

Before the optics of the Cassegrain design are discussed, there is one fundamental assumption to make about distant astronomical sources: incident light rays from such sources are considered as parallel rays, incident perpendicular to the plane of the telescope aperture.

Classical Cassegrain reflecting telescopes (Fig. 3c) were initially conceived by the French astronomer Guillaume Cassegrain are very popular in the field of optical astronomy, since extension of the effective focal length, f_0 of the system is able to be achieved [6]. As discussed in sections 2.1.2 and 2.1.3, increasing the value of f_0 causes a reduction in the field of view of a telescope and also provides a smaller image scale per pixel, so that the images observed by the telescope will be magnified by a larger factor and will correspondingly smaller section of the sky in greater detail. This makes the Cassegrain design a very suitable choice for the departmental telescope used for this project, as it enables students to observe smaller astronomical sources in more detail.

The Cassegrain design utilizes a concave objective, or primary mirror to reflect and focus light rays incident through a telescope aperture from an astronomical source to a prime focus point, F_0. A smaller secondary convex mirror situated along the objective optical axis causes the converging light

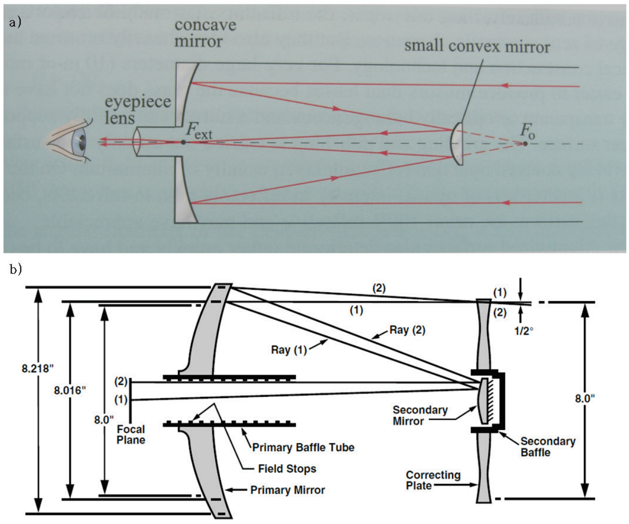

FIG. 3. *a:* Classical Cassegrain telescope setup. *b:* Meade LX-200 8$''$ Schmidt-Cassegrain setup, featuring an additional Schmidt corrector plate, over-sized objective mirror and primary baffle [1] [5].

rays to diverge, in turn extending the focal length of the system to F$_{ext}$, or f_0 as quoted in the characteristic equations in section 2.1. The diverging light rays continue to pass through a central aperture in the primary mirror, before reaching the focal plane of the system. If required, an eyepiece may be fitted with an integrated convex lens to bring the diverging rays parallel, enabling the lens in the human eye to focus the image obtained to the back of the human retina. For this investigation a CCD imager will take the place of the eyepiece and the diverging light rays will already arrive at the focal plane of the device, with no need for an eyepiece to perform further optical correction [5].

The physical distance between optical elements in a system and the focus is defined as the path length of the system. By applying a Cassegrain setup, the extended effective focal length is able to be contained within a comparatively short path length. This makes Cassegrain telescopes very practical, since the benefits of a longer focal length as afore discussed are able to be exploited, yet the telescope assembly is able to be retained in a comparatively small volume.

The telescope used in this investigation is of a Schmidt-Cassegrain design. The difference between a Schmidt-Cassegrain and classical Cassegrain telescope designs is the addition of a Schmidt corrector plate before the light rays are incident on the objective mirror. The Schmidt corrector plate is designed to correct for spherical aberration effects which would otherwise arise due to reflection from the concave objective mirror. Schmidt-Cassegrain telescopes are therefore referred to as catadioptric optical systems; ones in which both refraction and reflection of incoming photons is combined to achieve a focus on a focal plane.

The Meade LX200 Schmidt-Cassegrain setup can be seen in Fig. 3d. It should be noted that this diagram relates to a 8′′ aperture, although the setup is the same as for a 10′′ aperture.

Noticeable differences from the classical Cassegrain design in the LX200 Schmidt-Cassegrain design include the Schmidt corrector plate, an over-sized objective mirror and a primary baffle tube. The baffle tube is designed to cut out light rays outside of the field of view and improve the contrast of the final image. The Schmidt corrector plate causes light rays further from the optical axis to diverge, and therefore an over-sized primary mirror is included in the setup to 'capture' these rays. For a 10′′ Meade LX-200 aperture telescope, the over-sized primary mirror has a diameter of 10.375′′ [1]. By increasing the size of D_0, the light-gathering power of the telescope is able to be increased and the angular resolution limit α_c is reduced (Eqn. 1 & 4). This also makes the Schmidt-Cassegrain setup a sound candidate for use in this investigation, as fainter objects are able to be observed.

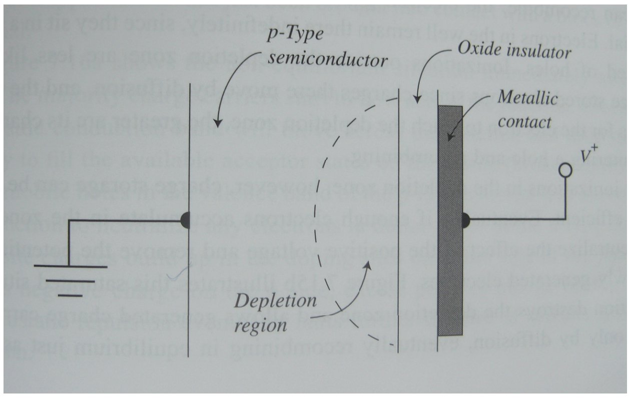

FIG. 4. Cross-sectional view of a MOS capacitor. Application of a V^+ potential to the metal layer generates a depletion region in the p-type semiconductor [9].

2.3 CHARGED COUPLE DEVICE

The Charged-Coupled Device, or CCD was first invented by Boyle and Smith at Bell Laboratories in 1969 [9]. Since its inception, it has become a popular imaging device in a variety of electronic applications, from scanners to video cameras. Due to this large industrial application, the cost of individual CCD devices has decrease such that in the field of astronomy CCD devices are able to be used as relatively low-cost detectors able to detect photon counts from astronomical sources. The CCD device takes the place of the eyepiece or human eye in the telescope setup; in order for a human to visually see the image taken by the CCD, the data has to be transferred to a computer device with a CCD imaging program such as ds9 or CCDOps [10].

The calibration of the KAF-0401E CCD used in this investigation was a significant portion of the project [11]. As the CCD had been dormant for a long period of time beforehand, its behaviour was not well understood. The project students therefore investigated and quantified the behaviour of the CCD pixels and identified different elements of data reduction which must take place when the CCD is used to collect astronomical data.

The theory behind the working of a shall be briefly discussed, including discussion of the different levels of data reduction which must take place when using CCD devices in an astronomy-based research environment.

2.3.1 METAL-OXIDE-SEMICONDUCTOR CAPACITOR

CCD devices consist of an array of Metal-Oxide-Semiconductor (or MOS) capacitors. The function of a MOS capacitor shall now be briefly discussed.

MOS capacitors (Fig. 4) consist of a sandwich of 3 layers: a p-type semiconductor block connected to electrical ground, an oxide insulator and a thin metal coating, or 'gate' to which a positive potential V^+ is applied. Typically the semiconductor is doped with Si and the oxide insulator is SiO_2. If SiO_2 is not used, the capacitor is referred to as a Metal-Insulator-Semiconductor (MIS) capacitor.

Without going into great depth about the working of this device, the application of a positive potential causes a depletion region, or potential well about the positively-charged gate. When an incident photon strikes the device, an electron-hole (e^- - h^+) pair is generated. The conduction-band e^- from this pair is attracted towards the metal gate, whereas the valence band h^+ travels out of the material to electrical ground.

The nature of the band structure of MOS causes these e^-s to remain in a filled 'well' by the positive gate, so long as a V^+ potential is applied to that gate. Throughout a given exposure, photons will continue to generate more and more e^-s about these gates on each CCD pixel. Once the exposure has finished, the CCD device then transfers the electrons between each date by alternating the V^+ applied to successive gates in a linear fashion.

2.3.2 FULL-WELL CAPACITY

There comes a point where the potential well for each pixel becomes "saturated" with e^-s. At this point, the pixel has reached "full-well capacity". Once full-well capacity has been reached, it is no longer possible to promote e^-s to the p-type valence band. Once this has happened, if further photons arrive at the device, a "blooming" effect occurs (Fig. **??**looming), whereby e^- physically overflow to adjacent pixel potential wells.

The number of electrons produced registered by a MOS capacitor increases linearly until the number of counts approaches the full well capacity of the device. At this point, it takes more photons to promote further e^-s to the p-type valence band. The response of the CCD to photons therefore no longer becomes linear and the device can no longer be used for accurate photometric readings. Typically, it is accepted that astronomical readings should contain counts no more than

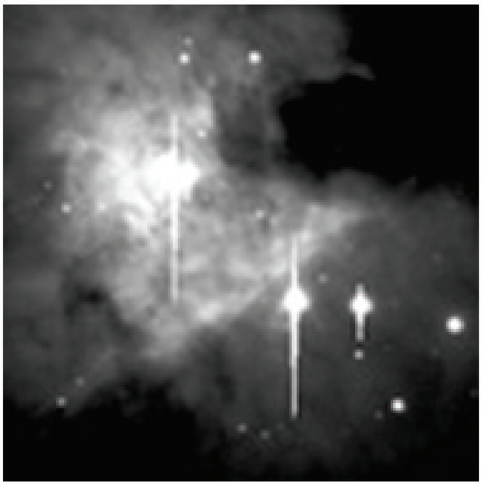

FIG. 5. Blooming, or overflow of e^-s occurring between adjacent pixels which have reached their full-well capacity [12].

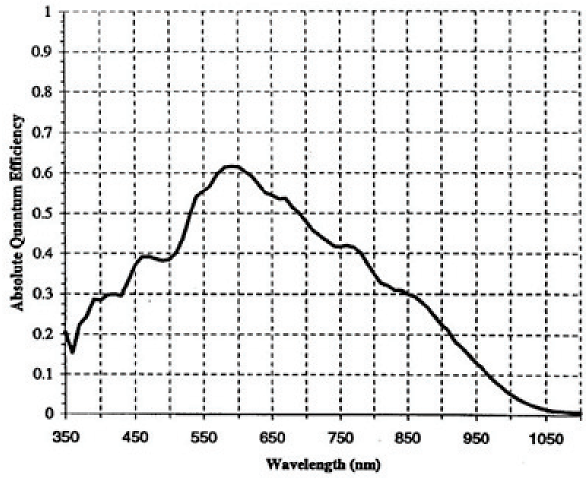

FIG. 6. The quantum efficiency response curve of the KAF-0401E CCD device [11].

half the value of the full-well capacity of the device to ensure accurate, linear photometric data. The full-well capacity value for the KAF-0401E CCD is 150,000 e^-s [8].

The gain of a CCD system is defined as the number electrons which are required for the output electronics of the CCD to register a count, also known as an Analogue-to-Digital Unit (ADU). For the KAF-0401E CCD the e^-/ADU value is 2.3, implying a maximum of 65,535 ADU counts which are able to be registered by any one pixel.

Flynn suggests that the Coldrick Observatory CCD device is linear up until approximately 40,000 counts [3]. This figure shall be re-assessed during this investigation.

2.3.3 QUANTUM EFFICIENCY

In theory, every photon which strikes a CCD surface should generate one electron. In reality however, this is not the case. The response of a CCD varies with the wavelength, λ of incident photons. Quantum efficiency is term used to quantifying the response of a CCD device to different λ . The quantum efficiency resopnse of the KAF-0401E CCD (Fig. 6 will be taken into account during the CCD data reduction process.

2.4 ASTRONOMICAL MAGNITUDE SYSTEMS

Astronomers use a historical magnitude system convention to quantify the brightness, or magnitude of a stellar object. The apparent visual magnitude, V_{mag} is defined as:

$$V_{mag} = \textit{-2.5*log(Flux) + k} \tag{5}$$

Note that a lower value of V_{mag} corresponds to a greater flux and therefore brighter object. The constant, *k* in this equation is defined as the zero-point magnitude constant. The value of *k* is set so that the magnitude scale has a zero reference point, i.e. every brightness measured can be measured relative to a known star's brightness (the 'zero-point'). Typically, the value of *k* is chosen so that the star Vega in the night sky corresponds to a magnitude value 0.

One of the aims of this investigation is to obtain a value for the zero-point magnitude offset, *k* which is necessary to apply to magnitude calculations from raw empirical flux values obtained from the Coldrick Observatory to perform accurate photometric magnitude calibrations for all sources observed.

The AB magnitude system is defined as:

$$AB_{mag} = \textit{-2.5*log(f) - 48.60} \tag{6}$$

Where the flux density, f is given in ergs s^{-1} cm^{-2} Hz^{-1}.

The AB magnitude system is utilized in the Sloan Digital Sky Survey (SDSS) multi-filter imaging study of the sky. An SDSS r′ filter has been purchased as a new addition to the LX200 telescope for the 2010/2011 project. Use of this filter enables standard SDSS r′ magnitude values to be calibrated against.

Fig. 7 depicts the transmission of the u′g′r′i′z′ filters used in the SDSS survey.

Fortunately, AB(r′) magnitudes equate to r′ magnitudes, therefore providing empirical fluxes from astronomical objects which are observed are converted to units of ergs s^{-1} cm^{-2} Hz^{-1} and substituted into equation 6, an instrumental r′ magnitude is able to be obtained.

This process in itself is rather simple and only involved basic algebra. The difficulty experienced by the project students was converting textbook V_{mag} and B-V_{mag} colour magnitude values obtained from the Hipparcos astronomical catalog into textbook r′ magnitudes to compare the accuracy of the r′ magnitudes obtained with [14].

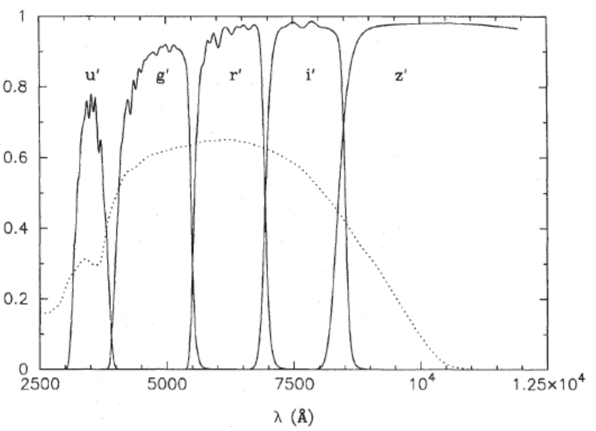

FIG. 7. Transmission functions of the u′g′r′i′z′ filters used in the SDSS survey [13].

A complex series of magnitude conversion equations was able to be devised using standard SDSS formulae to convert all the sources observed in this investigation to textbook magnitudes from their V$_{mag}$ and B-V$_{mag}$ Hipparcos magnitudes alone [15]. The equations can be found in full in Appendix E.

3 EXPERIMENTAL METHODS

3.1 CCD CALIBRATION

The majority of the project period focused on the calibration of the SBIG ST-7E CCD camera. The camera was initially placed on a bench surface in the Coldrick Observatory with a dust cover over the nose-piece to prevent any light from entering the device. In the first instance, series of exposures were taken to determine the typical dark current readings of the device. A number of characteristics were able to be quantified until it became apparent to the project students that there was in fact light leakage into the CCD device, so that light was able to enter the device despite the dust cap remaining being affixed. The whole calibration process was therefore repeated again in a dark room and further, more accurate analysis was able to be made in this environment.

The calibration process will be described in chronological order, commencing with calibration in the light-leakage environment.

3.1.1 'LIGHT-LEAKAGE' ENVIRONMENT

3.1.1.1 CCD OPERATING TEMPERATURE

CCDOps software was used to operate the SBIG ST-7E CCD device for the duration of the project. It was imperative that the CCD was kept as cool as possible to ensure that dark current and other forms of noise were kept to a minimum during CCD operation. A value for the operating temperature therefore had to be found at which the CCD device could comfortably work at.

The CCD is able to be cooled via a fan attached to the device, controlled through CCDOps. The first thing which became immediately apparent to the project students was that the temperature displayed on the CCDOps user interface fluctuated between approximately $\pm$ 0.6° around the value set. For example, if the CCD was set to operate at $-5°$C, the value displayed may fluctuate between $-5.3°$ to $-4.6°$ C. It was found that the amplitude of this fluctuation was constant no matter what operating temperature was chosen. Whatever the reason behind these fluctuations on CCDOps, the consistent fluctuation can be quantified as a systematic error within the CCD cooling system and is therefore not a concern, since all operating temperatures will perform in the same manner relative to each other.

CCDOps also displays the $\%$ capacity the CCD fan is operating at in order to maintain the temperature set by the user. It was found that at typical room temperature conditions in the Coldrick Observatory of 15° C, the CCD was able to reduce the operating temperature down to approximately $-15°$ C at which point it was working at 100$\%$ capacity. This is consistent with the value quoted by SBIG: "30$\%$C lower than the ambient room temperature" [8].

To allow for fluctuations in room temperature and also to ensure the CCD was working at approx 60-70$\%$ capacity during operation to allow room for leeway, an operating temperature of -5$\%$ C was used to obtain all CCD calibration data, unless otherwise stated. This operating temperature was also used on observation nights, so that the CCD calibration performed in the laboratory environment could be applied to the empirical data obtained.

3.1.1.2 DARK FRAMES

'Dark' exposures of varying lengths were initially taken, with an aim to producing a master dark frame which could be scaled and subtracted from empirical data. Various exposure lengths were taken, and IDL was used to plot the histogram function obtained from dark current pixel counts.

If many exposures of the same length are taken, IDL is able to average these frames and produced a "median" frame. This is a useful technique, since anomalies caused from cosmic rays or other defects are able to be accounted for and will not affect the value of the median array. A brief outline of this technique will be discussed.

IDL is able to read in the FITS files generated by the CCD camera and assigns each pixel value to an array of size 765x510. IDL is able to store a value for each point on the array. The notation for such an array in IDL programming language is `array=[765,510]` . It is possible to instruct IDL to just focus on one of these pixels, for example `array[0,0]` would refer to the pixel in upper-left corder of the array, i.e. in the first row and first column. `array[1,0]` refers to the neighboring pixel to the right in the first row; `array[0,1]` refers the neighboring pixel below in the same column and so on. IDL is then programmed to median each individual pixel value from subsequent exposures into a median frame.

As an example, if 7 images were taken, IDL would generate 7x [765,510] data arrays. Each array would have a different value for the `[0,0]` pixel. IDL is instructed to look at each of these values, calculate the median value and output this number as the pixel value for the `[0,0]` pixel in a new, "median" array. Full IDL code for this process can be found in Appendix B.

The median array generation method was used to obtain median dark frame files. Since the signal-to-noise wanted to be kept to a minimum, longer dark-current exposure lengths were preferable. In addition, if more input files were introduced to the median routine,the noise Poisson counting statistical noise was able to be reduced in the final median frame.

Since it is possible to scale a master dark frame down to the dark current exposure length required, median dark current files of up to 30min in length were generated. Using the `plot, histogram(array)` function, IDL was used to plot a histogram of frequency vs counts for the median dark files generated.

3.1.1.3 BIAS FRAMES

Before the dark current histograms were able to be analyzed, the bias noise for the CCD device had to be accounted for. The bias noise is theoretically the frame which would be generated from a 0s dark current exposure. This was not practicable in the laboratory environment, as the shortest exposure able to be operated through CCDOps was 0.12s. It was however deduced that the mean of the dark current accumulated in 0.12s was of the order of fractions of a count, so would change the 0.12s exposure by a minute amount, if at all.

20x 0.12s bias exposures were therefore taken and generated into a median "master bias" array. This array was subtracted from all median master dark files generated. The median bias array (Fig. 8) showed a large amount of structure. This is due to the CCD readout process; pixels are being read out in the top-right hand pixel in the Fig. 8 ds9 images (NB: ds9 actually flips images vertically, so this is actually the bottom-right pixel of the physical CCD array). As each pixel is read out, read-out noise is generated which causes pixels nearer the readout pixel to obtain more counts than they actually received, as the readout process passes electrons through them at a rapid rate

This structure will always be present in any CCD image taken. It's consistency means that this master bias array can simply be subtracted from all images taken by the KAF-0401E CCD device to obtain more accurate data. Fig. 9 demonstrates

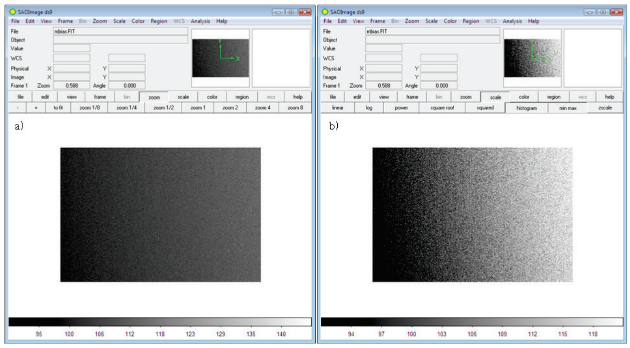

FIG. 8. The master bias from the from Coldrick Observatory KAF-0401E CCD device. *a*: linear scale. *b*: histogram scale, showing a large amount of structure from left-to-right across the CCD array.

the effect subtracting the bias frame has on the dark current histogram.

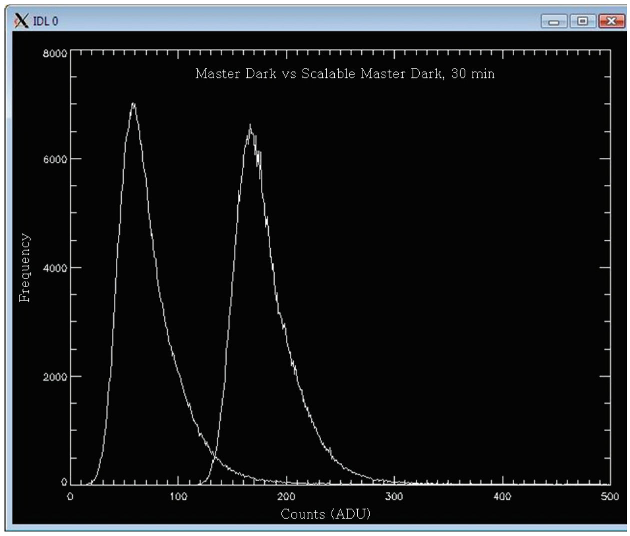

FIG. 9. Comparison of the histogram plot for the master dark and scalable master dark (bias subtracted) frames. The right-most plot represents the master dark frame. The jagged edges of the plot are a result of structure inherent in the bias readout noise. By subtracting this bias frame, the function on the left is able to be produced. Note that the lines of the plot are smoother, indicating the removal of the bias structure. The mean of the scalable peak has also been reduced, as the bias frame produces a mean value of approximately 100 pixel counts.

3.1.1.4 DARK CURRENT LINEARITY VS TIME

The subtraction of a master bias from a master dark frame produces a scalable master dark frame. Since the bias has been accounted for, if for example a 30 minute scalable master dark frame were to be used to subtract 60s worth of dark current from an exposure, the scalable master dark frame would simply have to be divided by 30 to equate it to a one minute exposure and could then be subtracted from the exposure frame.

For this theoretical model to hold, one assumption has to be made: the dark current of the CCD is linear with time. The linearity of dark current vs time was therefore investigated to ensure the relationship was as expected.

3.1.1.4 BAD PIXELS

Dark current is a Poisson distribution. The pixel counts received during dark current calibration are sufficiently large that the Poisson distribution from these measurements should theoretically take the form of a Gaussian-shaped distribution. As can be seen from the histograms in Fig. 9, this evidently not the case.

The most obvious factor which deviates from a traditional Gaussian distribution is the 'tail' at the upper end of the distribution. This tail is as a result of bad pixels. Bad pixels are defined as pixels which do not behave in the same manner as an average CCD pixel. This investigation focuses on three types of bad pixel:

1) *Hot pixels:* Hot pixels accumulate charge faster then the the average CCD pixel, producing pixel values significantly higher than an average CCD pixel.

2) *Warm pixels:* Warm pixels behave in the same way as hot pixels, but the charge accumulation is less dramatic and therefore the final pixel values are marginally higher than an average CCD pixel.

3) *Cool pixels:* Cool pixels behave in exactly the opposite way as warm pixels: the pixel values they produce are marginally lower than that of an average CCD pixel.

The effect of hot pixels causes the most dramatic effect on a CCD histogram pilot, and as such this was the first class of bad pixel which was investigated.

Fig. iteration depicts a 30 min dark frame with a log x & y axes to highlight a significant secondary peak in the distribution. Note that this peak is not present in Fig. 9 due to the x-axis range.

The secondary peak present in Fig. iteration is as a result of hot pixels. The pixels contained within this peak give significantly greater pixel counts than the average pixel distribution in the frame, which constitutes the first peak in the figure. It was concluded that the pixels constituting the secondary peak had to be corrected for in some way.

In order to do this, the co-ordinates of the hot pixels themselves had to be identified by IDL. To identify a "hot" pixel a cut-off value had to be determined. The Rose criterion, named after Albert Rose states that a signal-to-noise ratio of 5σ is necessary to identify an object with 100% certainty [16]. It was therefore concluded that the standard deviation, σ of the primary peak would be identified and any pixels above a value 5σ would be identified as "hot" pixels. In order to perform this procedure, an iterative IDL program was written which used

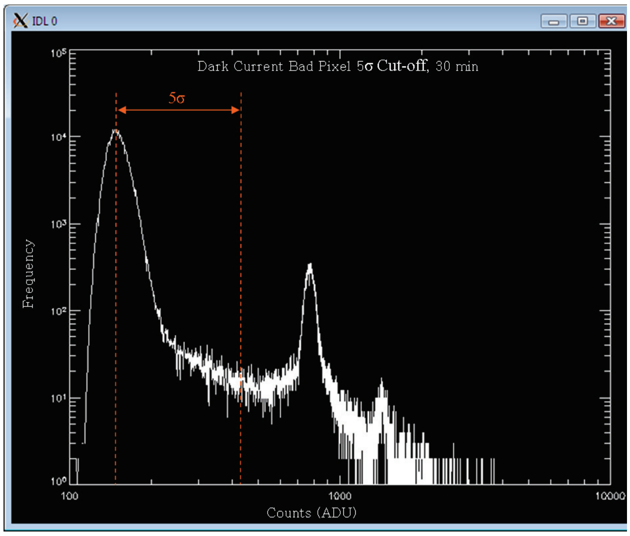

FIG. 10. 5 σ cut-off limit to eliminate hot pixels, which cause the secondary peak in this plot.

an initial guess of the cut-off point and calculated the corresponding σ value to the left of this point. The output 5 σ value would then be used as the next cut-off assumption and so until the procedure converged at a constant cut-off value. The full IDL code for this procedure is given in Appendix C.

The above process is also known as "sigma-filtering". The filter chosen in this case is a 5 σ filter which is applied to the image. IDL can define the "hot" pixels as `array[where(array gt 5*σ)]`. Once the co-ordinates of these hot pixels had been identified, a masking technique was able to be applied to account for their statistically anomalous values.

"Masking" implies generating a pixel mask which is an array of the same dimensions as the original array with values of 1 and 0. The co-ordinates of the hot pixels as identified by IDL dictate which pixels in the mask are given a value of "0". Since the remaining "good" pixels maintain a value of 1 in the mask, the mask is then able to be multiplied by the original image. This process is called "masking" the original image. In this case, the original image is "5 σ masked", which simply sets the value of every identified hot pixel to 0, whilst leaving every good pixel value unchanged. Fig. 11 demonstrates the resulting histogram after a 5σ mask has been applied.

As can be seen in Fig. 11, a tail still exists on the histogram which distorts its shape away from a theoretical Gaussian distribution. This smaller 'tail' is a result of warm pixels; these are addressed further in section 3.1.2.

3.1.1.5 LIGHT LEAKAGE

In the process of taking additional 30min dark exposures to reduce the noise in the master dark frames produced and thereby better quantify its behaviour for the CCD device, three 30min exposures were taken as the sun was setting on 13 Dec

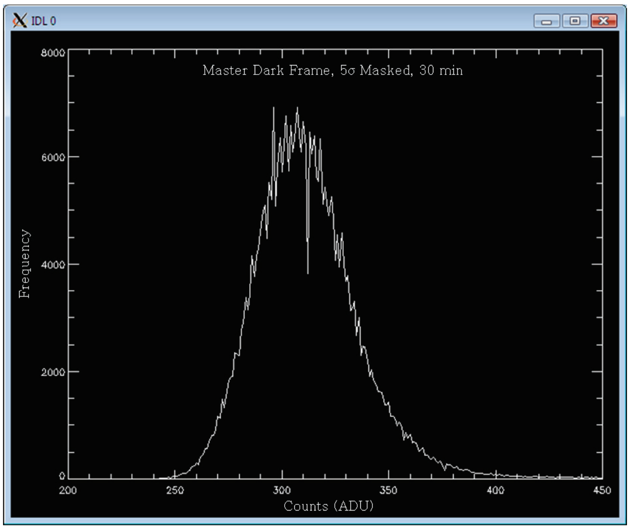

FIG. 11. 30 min master dark frame, after a 5σ mask has been applied. Note that the bias frame has not been subtracted from this image.

2010. The Coldrick Observatory has glass windows, so the ambient light conditions on this day reflected that of the outside sky. Fig. 12 compares the mean counts observed from these 30min dark frames with the time of day the images were taken .

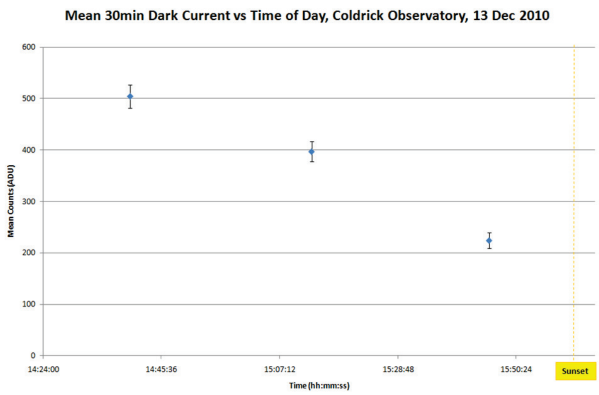

FIG. 12. The relationship between three 30min dark frame mean counts and the time of day on 13 Dec 2010. Sunset took place at 16:01 on this date [17]. The vertical error bars are calculated from the error in the Poisson counting statistics, $\sqrt{N}/N$.

As Fig. 12 clearly demonstrates, the Coldrick Observatory SBIG ST-7E CCD device is susceptible to light leakage, despite a dust cover being placed over the nose-piece to prevent light from entering the device. The 30min dark frame mean pixel counts values should have remained constant between subsequent exposures, within the quoted $\sqrt{N}/N$ error, however this was not found to be the case.

This conclusion therefore drove the project students to restart the CCD calibration process in a dark room, simulating the environment the CCD camera would be exposed to when attached to the Meade LX-200 telescope on an observing night.

3.1.2 'DARK-ROOM' ENVIRONMENT

The dark room CCD calibration repeated all the the steps mentioned above. It was found that subsequent 30min dark exposure mean counts remained constant with time, as expected - indicating that more accurate calibration was able to take place. Further calibration procedures undertaken in the dark-room environment shall now be discussed.

3.1.2.1 DARK CURRENT LINEARITY VS TEMPERATURE & TIME

The relationship between dark current and time was investigated by taking a number successive dark current exposures of length 5s, 10s, 20s and 30s. This procedure was then repeated using the CCD at a variety of operating temperatures: -5°C, 0°C, 5°C, 10°C and 15°C. The results obtained showed a strong correlation, showing the clear benefit of choosing a low CCD operating temperature and providing strong evidence to suggest that 5°C is a good CCD operating temperature to operate at for calibration purposes. These results are further discussed in the results section.

3.1.2.2 WARM & COOL PIXEL MASKING

As previously discussed, the plot in Fig. 11 still contains pixels which distort the theoretical Gaussian distribution which should be obtained. A theoretical Poisson distribution was fitted to this curve with the same central and standard deviation parameters to match the main peak. The GAUSS2DFIT command in IDL is a very useful resource to enable such fits to occur.

As a result of the theoretical fits to the empirical data, it became apparent that 2 'tails' actually exist in Fig. 11 after 5σ masking - the tail to the right is due to warm pixels and the smaller tail to the left is due to cool pixels. A simple sigma mask will no longer be able to remove these pixes, as doing so would also begin to remove good pixels.

A new method was therefore devised to identify warm and cool pixels. Mathematically the odds of a single 'good', or well-behaved pixel value falling above the mean of a Gaussian distribution is 0.5. Repeating another observation to produce a second Gaussian distribution, the same pixel has another 0.5 probability of falling above the mean. The probability that it has fallen above the mean in both cases is $0.5^2 = 0.25$. It is possible to calculate the number of independent observations which would need to take place in order for the possibility of a good pixel to have fallen above the mean every single time to be reduced to such a low value that none of the good pixels in the device would statistically fall above the mean in ever observation. This calculation is outlined in equation **??** below.

$$Total\ No.\ of\ Pixels\ in\ Array = 765 * 510$$
$$0.5^x = \frac{1}{(765 * 510)}$$
$$x = \log_{0.5}\left(\frac{1}{(765{*}510)}\right)$$
$$x = 18.57 \tag{7}$$

19x 30min dark current exposures would therefore have been sufficient in a dark-room environment to ensure that the probability was sufficiently small that no good pixels could have statistically fallen above the mean for every single observation made. 20x 30min dark frames were therefore taken to ensure a margin for error for cosmic rays hits or other anomalies in one of the frames.

Pixels which fell above the mean in every single exposure were labeled as ”warm pixels”. To be precise, the previously identified hot pixels would also fall within this bracket; the warm pixels themselves are those which were not previously identified as hot pixels.

Of course, the above method can be applied in reverse; those pixels which fell consistently below the mean in each exposure were labeled as ”cool” pixels.

As a result of this process, three ’levels’ of masking were now able to be quantified:

1) *Hot masking:* Simply masking the hot pixels

2) *Warm masking:* Masking both the hot pixels and warm pixels

3) *Cool masking:* Masking the hot pixels, warm pixels and cool pixels

The effect of these different levels of masking on 30min darkroom data is shown in Fig. 13.

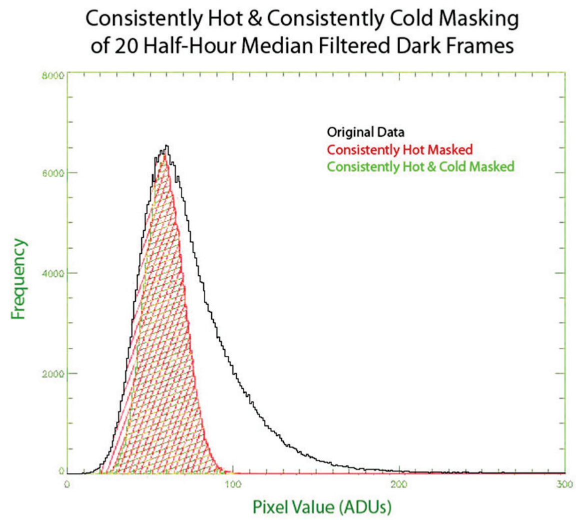

FIG. 13. The distribution functions observed when a bias-subtracted 30min median dark room exposure is masked using progressively rigorous hot, warm and cool masking methods. Each subsequent masking method causes the distribution to more closely model a Gaussian shape. Credit to W. Foxall for use of this image.

3.1.2.3 FIXING BAD PIXELS

Now that a variety of methods to identify different levels of bad pixels was established, project students investigated methods whereby bad pixel values would be able to be corrected instead of simply set to zero. This was particularly relevant for the heavier masking methods, since a significantly higher proportion of the pixels were masked in each case; hot masking masks ~ 10 %, whereas cool masking masks ~ 45 % of the pixel array.

An IDL procedure (.pro) was independently written and cross-checked by both project students to enable bad pixels to be fixed. The procedure identified bad pixels depending on the input mask provided by the user. It then searched for good pixels surrounding the bad pixel and replaced the value of the bad pixel with the average value of its neighboring pixels. The procedure is iterative and repeats itself, prioritizing bad pixels with greater availability (i.e. a greater number of good pixels surrounding them) until all bad pixels have been fixed. The procedure the author wrote to perform this task is entitled `fixbadpixel.pro` . The full code and flowchart for the procedure can be found in Appendix C. Fig. fixbadpixel summarizes the function of the `fixbadpixel.pro` procedure.

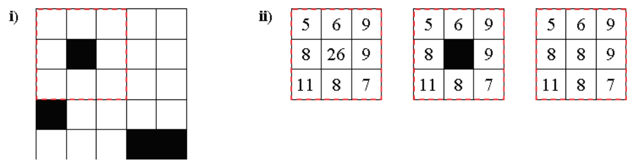

FIG. 14. The function of the `fixbadpixel.pro` procedure. *i:* Sample 5x5 array mask, where black pixels represent bad pixels and white pixels represent good pixels. In this case, the bad pixel with 8 good pixels surrounding it would be fixed first by the routine, followed by the bad pixel with four good pixel neighbors followed the two in the lower-right hand corner of the image, the left-most bad pixel being fixed first. *ii:* The red dotted square in from figure *i* is observed to demonstrate the fixing of an individual pixel. In this example the central pixel is bad and therefore has a statistically anomalous value; in this example its value is significantly higher then its neighbors. Once masked, this value becomes 0, represented by the black square in the second step. The third step is the pixel fixing process; the `fixbadpixel.pro` procedure will calculate the mean of the good pixels surrounding the bad pixel, in this case 7.875. This value will be rounded up or down, in this case to 8 and will replace the bad pixel value.

3.1.2.4 FLAT-FIELDS

Flat-fields were the final stage in the CCD calibration process. Flat-fields are used by astronomers to correct for optical effects that may arise in a image, for example aberrations in the image or an uneven focus of light intensity across the CCD field of view. To correct for these effects, a flat field was able to be generated by attaching the SBIG ST-7E CCD device to the Meade LX200 eyepiece and defocus the telescope so that it could be pointed at a plain wall inside of the Coldrick Observatory viewing dome.

Flat-field exposures should peak at around half the full-well capacity of a given CCD device. Exposures were therefore taken so that a maximum of 30,000 ADU counts were obtained. This setup also allowed investigation into the photon linearity of the CCD device, so exposures of increasing length were also taken until CCD saturation for this purpose.

Once a suitable flat-frame image has been obtained, it is then normalized so that its maximum value is equal to 1. Exposures taken can then be divided by this normalized flat-field to generate a flat-field corrected image. Flat-fields should be taken on the night of an observation, as they correct for dust particles, which may have appeared since a previous observing session. Fig. 15 depicts the normalized flat-field taken before the observing session on 07 March 2011.

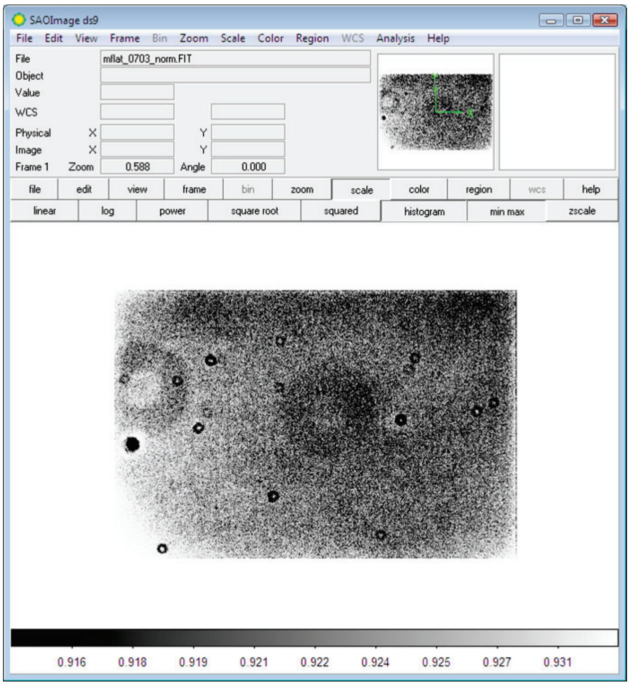

FIG. 15. Normalized flat-field image taken before the observing session on 07 March 2011. Notice the dust doughnuts of various sizes which form around particles of dust which lie both extrnally and internally to the telescope and CCD device. There is also a slight gradient of illumination present in the flat-field.

3.2 DAY TRIALS

Once the calibration and behaviour of the SBIG ST-7E CCD device itself was well understood and characterized, day trials had to be performed to test the CCD operation in unison with the Meade LX-200 telescope setup. Initially, project students practiced aligning the view-finder of the Meade LX-200 device and focusing the telescope using the focus knob at the back of the telescope. Ground-based objects were used for these focusing experiments. Once focus was achieved using an eyepiece attachment, it was removed and replaced with the SBIG ST-7E CCD device. CCDOps has a ”focus” mode which allows rapid low-resolution images to be taken and allows the user to focus the telescope whilst observing the readout images from the CCD device.

It was found that by rotating the focus know 1 1/4 turns counter clockwise once optical focus had been achieved with the telescope eyepiece, the setup was such that the CCD device was approximately in focus. CCDOps focus mode could then be used to fine-tine the focusing. The focusing technique required a lot of practice and was a skill which was invaluable to the project students during observing nights.

Basic telescope operations and use of the Meade handset were accustomed to by the students, so as to ensure fluid transition and efficient use of the telescope during observing nights.

3.3 NIGHT OBSERVATIONS

Two observing nights were used to collect the astronomical data for this project: 07 March 2011 and 24 March 2011. These nights were the first opportunity for the students to apply the skill-sets practiced during the day trials in a night-time environment, so a steep learning curve was necessary. Typically only 4-5 observing hours were available on each night, emphasising the importance of being efficient and adept with the equipment.

Golding presents a quick start guide discussing how the Meade LX-200 device is able to align with known stars [2]. Huyton discusses the RA/Dec co-ordinate system used to locate objects in the night sky [4]. The specifics of these topics shall not be discussed further here, other than to stress their importance to the user.

1/2-star alignment was an important process to perform accurately, since inaccurate initial alignment meant that the tracking of the telescope would soon become inaccurate, leading to streaked images. It was noticed that the tracking possible with the Coldrick Observatory setup is very sensitive to movement. If student accidentally knocked the vertical pole the telescope is situated on or caught on a cable, for example the telescope would lose its tracking capability more rapidly. The telescope also only attached to the base below by one screw. This is a systematic factor which prevents the device from tracking as well as it could do.

The telescope was able to observe bright, known objects well. It soon became apparent that for fainter objects which are not able to be seen by the naked eye, the ”go-to” function

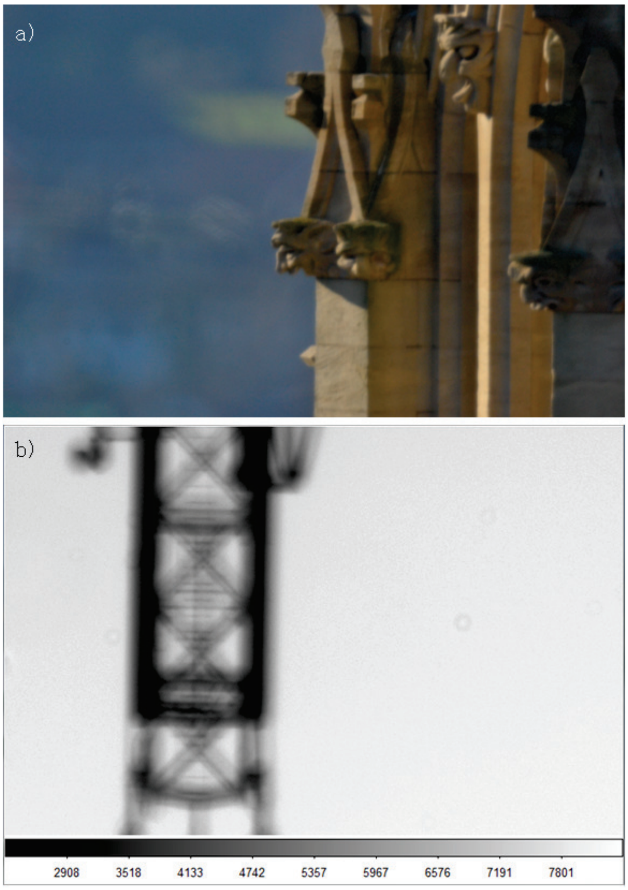

FIG. 16. Ground-based targets used to practice focusing on, both optically and with the SBIG ST-7E device. *a:* Gargoyle head on the Wills' Memorial Building. *b:* Purdown BT Tower, situated in the Lockleaze suburb of Bristol. Visible in the far distance NE of the Coldrick Observatory.

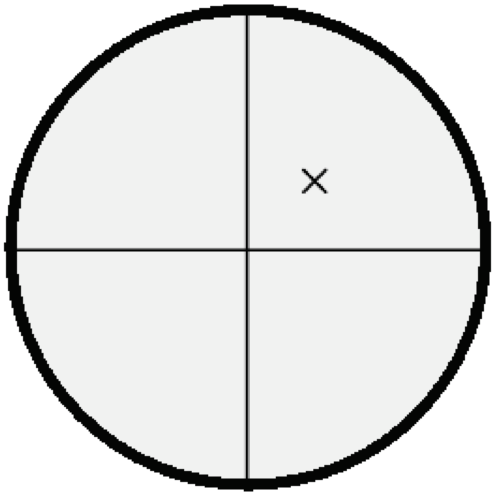

FIG. 17. A typical phenomenon observed as a result of bad telescope tracking: when instructed to slew to a given R.A./Dec to centre object 'X' in the scope, the finder scope would lie some distance away from the object. Manual slewing was therefore necessary with the Meade handset in order the centre the target star. Of course, correct alignment between the telescope and finder scope is necessary for this corrective procedure to be accurate.

of the telescope did not always centre the scope on the source required, as depicted in Fig. 17.

A further problem was that the RA/Dec object library of the telescope did not correlate with either the J2000 or J(of date) RA/Dec systems present in Stellarium, the primary software program used to assist students to identify and locate objects in the night sky. The students were able to devise an "offset" method to account for this inaccuracy: the Meade LX-200 telescope was instructed to slew to a known stellar object. Once centred on what the telescope thought is this object, the RA/Dec reading of where the telescope *thought* it was pointing was recorded. The telescope was then manually adjusted so that the known stellar object was actually in the centre of the field of view of the scope. The new RA/Dec reading was recorded. The difference in these readings was referred to as the "RA/Dec" offset necessary to calibrate co-ordinate systems between Stellarium and the Meade LX-200 control device.

The offset method proved very successful, and enabled the project students to locate the 9.76 r'_{mag} Standard star, HIP 31635 used as a key photometric calibration source in this investigation.

4 RESULTS AND DISCUSSION

4.1 CCD LINEARITY VS TEMPERATURE & TIME

Fig. 18a demonstrates that the behaviour of the SBIG ST-7E CCD device is linear with time, with respect to dark current. This therefore concludes that generating scaled master dark frames, as described in section 3.1.1.4 is a suitable method of data reduction. Fig. 18b and 19 demonstrate that the value, standard deviation and structure of the bias also increase as the operating temperature increases. A minimum bias value with a small standard deviation is preferable, which is strong evidence to suggest that low temperature CCD operating temperatures produce more accurate results.

It was possible to have the CCD work as an operating temperature of $-10°$C, however this would have dramatically increase the % capacity the device would be working at and as can be inferred from Fig. 18a, the difference in the bias value as a result of this would have been minimal. If a CCD is working at near maximum capacity, the operating temperature may not be able to remain constant at $-10°$C if ambient temperatures were to fluctuate. This is therefore strong evidence to support the choice of a $-5°$C CCD operating temperature in the Coldrick Observatory environment.

It is also worth noting that the low gradients at cooler temperatures from Fig. 18a indicate that the dark current value for a bias exposure length would be very minimal indeed, therefore supporting the assumption made in section 3.1.1.3 that the signal obtained in a 0.12s exposure is due to bias, or read-out noise in its entirety.

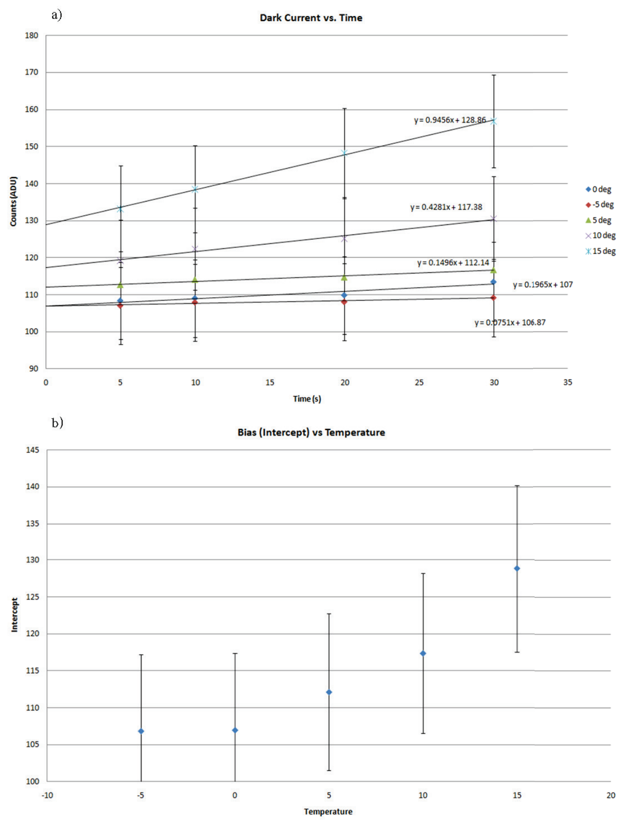

FIG. 18. Demonstration of the behaviour of the linear behaviour of the SBIG ST-7E CCD device with time. *a:* Demonstrates the linear behaviour of the CCD holds at various operating temperatures. *b:* The y-axis intercept from figure *a* is the mean of the bias frame taken at that particular temperature, whose value increases for greater temperatures. Figure 19 describes the shape of the bias distribution at each temperature, also. Errors due to Poisson counting statistics.

Fig. 21 is significant in that is proves that the CCD linearity relationship also holds with photons. This is a significant point to note in the calibration process, as photons may not behave the same as dark current and so the latter linear relationship cannot be assumed for photons. Fig. 21 bears resemblance to that presented by Flynn [3], suggesting that project students were correct to only perform data analysis on frames with a maximum of 40,000 ADU counts or less, to ensure the CCD is still behaving linearly at this limit.

4.2 APER PHOTOMETRY

4.2.1 COMPARISON OF MASKING METHOD

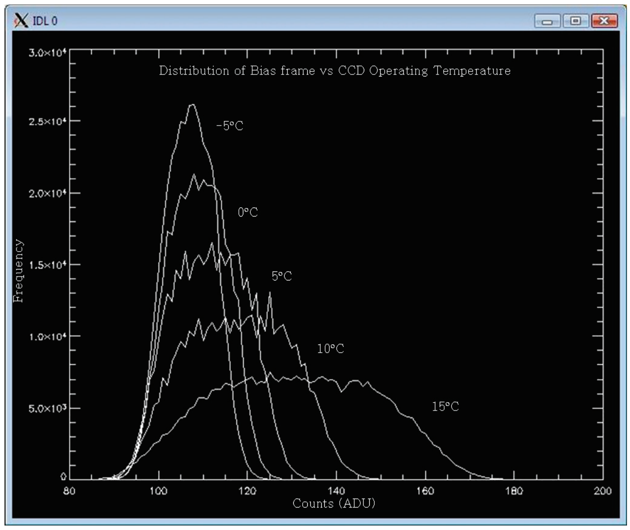

FIG. 19. Demonstrating the shape of the bias distribution with increase in CCD operating temperature. An increase in CCD operating temperature causes the mean, standard deviation in the structure to increase. The more jagged edges present at higher temperatures indicate a more dramatic structure gradient in the bias frame.

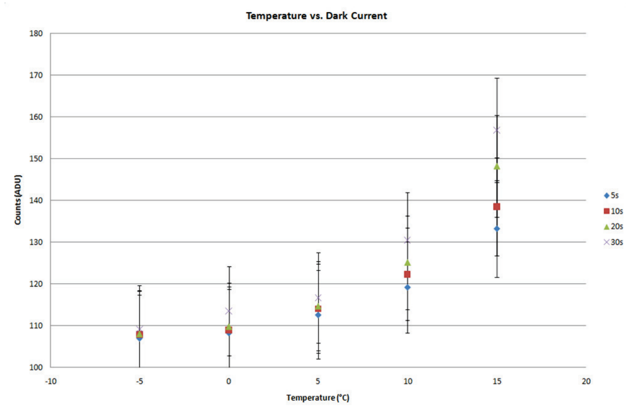

FIG. 20. Demonstration of the behaviour of the CCD with temperature. The dramatic exponential increase in counts as the temperature is increase highlights the necessity to maintain the CCD at a low operating temperature. Vertical error bars due to Poisson counting statistics.

Fig. 22 demonstrates the effect of applying successive masking methods, and subsequently running `fixbadpixel.pro` on two stars of considerably different r′ magnitudes: 9.76mag$_{r'}$ and 4.32mag$_{r'}$ for the r′ standard HIP 31635 and Maia, respectively.

From Fig. 22a it is immediately apparent that the data for which the bad pixels have been fixed provide a lower flux count than the raw, unfixed data. This is because for dimmer sources, the statistically anomalously high hot pixel values significantly increase the flux received from the star, thereby resulting in it appearing brighter on the CCD device than it should do. This concludes that for dimmer sources, it

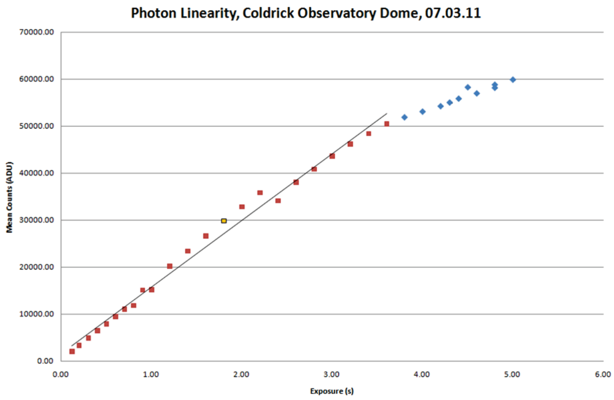

FIG. 21. Demonstrating the linearity of the SBIG ST-7E CCD device with photon incident photon counts up until approximately 50,000 ADU, where the linear relationship begins to level off as the full-well capacity of the device is reached. The points labeled in red constitute contribute towards the linear best fit line included on the plot. The points labeled in blue demonstrate non-linear behaviour. The data point highlighted in yellow at an exposure of 1.8s indicates that this was the exposure used to generate the normalized flat field frame for the 07.03.11 observing night. Vertical error bars are included on the graph due to Poisson counting statistics, however these are not visible on the scale of this graph.

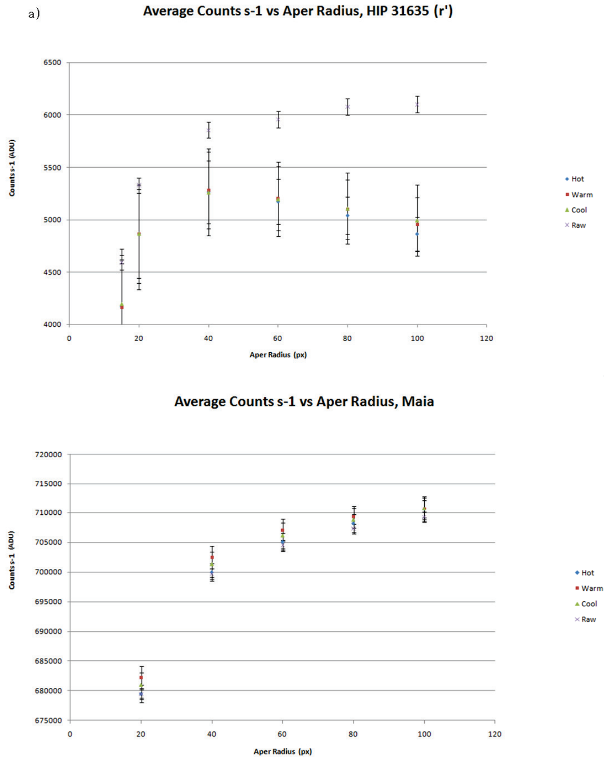

FIG. 22. Results from Aper circular photometry on *a:* HIP 31635 (r′) and *b:* Maia. In each case the exposure length was scaled to 1 second. It can be seen that for dimmer sources such as HIP 31635, the choice of mask does not vary the magnitude obtained significantly. It is however important For brighter sources such as Maia the difference is less apparent, unless cool masking is introduced, where the difference is more significant. Vertical errors due to Poisson counting statistics.

is important to mask bad pixels to some degree and run the `fixbadpixel.pro` procedure on the image, as more accurate flux values are able to be obtained by doing so.

Fig. 22b suggests that for brighter sources such as Maia, masking does not significantly alter the flux received. Each successive masking method has little effect on the flux obtained, and the values are no different from that of the raw, unfixed image (within the quoted Poisson counting statistic error).

Fig. 23 demonstrates the errors obtained from the circular Aper process performed on Maia. As the level of masking becomes more severe, the flux error from the Aper process increases: the error in the flux is calculated from $\sqrt{N}/N$ for the good pixels within each aperture radius. As the number of good pixels decreases, the fractional $\sqrt{N}/N$ also increases thereby generating a larger error th results obtained from each successive masking method.

As a result of the Aper photometry process, it can be concluded that for dimmer astronomical sources, it is crucial that hot masking be applied to the raw data and the hot pixels should be fixed using `fixbadpixel.pro` . It is not necessary to perform either warm or cool masking in this instance, as the values obtained do not differ within the error limits.

For the case of brighter objects, no masking or hot pixel fixing is necessary. Again, warm and cool pixel fixing will also not alter the photometric results obtained outside of the quoted error limits.

It was therefore concluded that hot masking and hot pixel fixing with `fixbadpixel.pro` would be performed on all astronomical objects observed. This method thereby ensured accurate flux calibration for dim objects, and although not strictly necessary for brighter objects would produce an accurate flux value for these sources also.

This was a very significant conclusion of the calibration process, and enabled r′ photometric calibration to be performed in full, as detailed in section 4.2.2.

4.2.2 r′ PHOTOMETRIC CALIBRATION

As a result of the Aper photometry on HIP 31635 and Maia, it was concluded that hot masking and pixel fixing would be performed on all empirical astronomical data. This enabled a further IDL routine to be written to enable raw data to be fully reduced, entitled `data_reduction.pro` . The basic function of this procedure is shown in Fig. 24. Note that the `fixbadpixel.pro` procedure is embedded as part of the `data_reduction.pro` code. Full IDL code for the `data_reduction.pro` procedure can be found in Appendix F.

Once reduced data was obtained for all astronomical sources measured, Aper photometry could be performed on

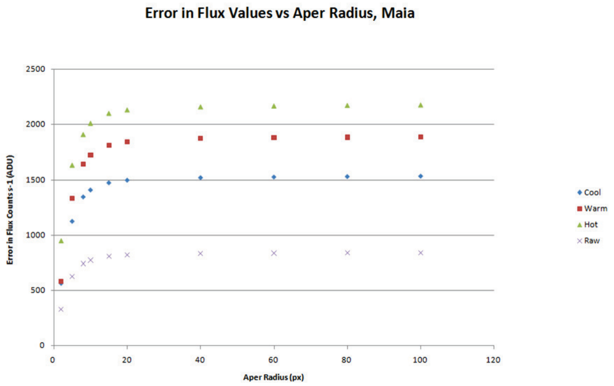

FIG. 23. Demonstration of the increase in the error in the flux obtained via the Aper process as the level of masking increases. This is due to the decrease in the number of ’good’ counts *N* as more masking is introduced, thereby increasing the Poisson counting statistical error.

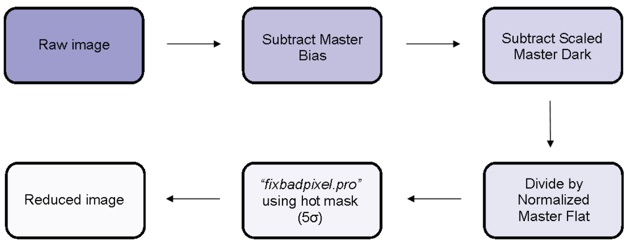

FIG. 24. The data reduction process performed by the `data_reduction.pro` procedure.

each source. The maximum flux value provided from the Aper photometry process was measured and converted to an instrumental r′ magnitude. Appendix G provides a full observation summary of all objects taken and the corresponding instrumental r′ magnitudes obtained.

The instrumental r′ magnitudes were able to be corrected for quantum efficiency effects at the centre of the r′ waveband, 626 μm and scaled up by a factor of 2.3 so that the ADU counts obtained related to the correct number of incident photons to obtain a corrected r′ magnitude for each object. It was observed that the corrected r′ magnitudes differed in value from the theoretical r′ magnitudes by a similar factor for every object observed. The mean ′ corrected instrumental - r′ theoretical magnitude values obtained was 3.03 ± 0.16.

There is one other calibration factor which has not been considered here: atmospheric extinction. A plot of instrumental r′ magnitude and airmass was attempted to be made for each object observed. The plots did not follow the expected relationship, due to the very short variation in airmass across which multiple observations of an object were made. To try and utilize the fact that different objects were observed at a variety of altitudes in a given observing night, a plot was attempted to me made by normalizing the magnitude of each object and plotting them on a common airmass x-axis. Fig. 25 demonstrates the result of such a plot, reducing the magnitude of both Maia and HIP 31635 (r′).

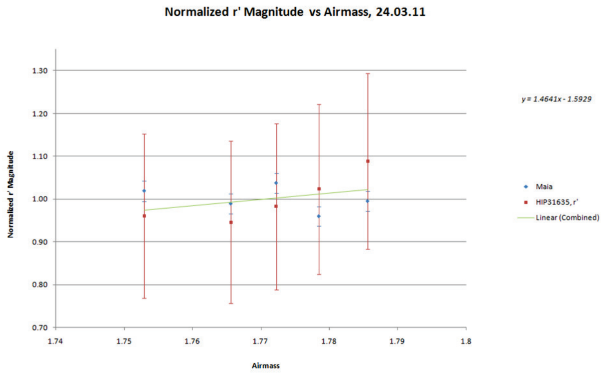

FIG. 25. Plotting normalized r′ magnitudes for both Maia and HIP 31635 (r′) vs airmass on the same x-axis. This demonstrates that an accurate extinction plot was not able to be made by using different sources on a plot with the same x-axis. Vertical error bars due to Poisson counting statistics vary with length of exposure taken, with the result that a best fit line wasn’t able to pass through every error bar. The only solution to plot an accurate instrumental r′ magnitude vs airmass graph is to repeat observations of the same object over a wide range of airmass values, so that the error bars remain proportionally the same for each data point on the graph.

This method was unable to produce accurate results as a best fit line was not able to be drawn through every error bar of the plot. Again, a greater airmass x-axis variation is required for a more accurate extinction plot to be made. Until such a plot can be made, the extinction coefficient, κ for a given observing night cannot be obtained.

It can however be shown that the corrected instrumental - theoretical r′ magnitude differences obtained are proportional to airmass, as Fig. 26 demonstrates. This suggests that a zero-point r′ magnitude calibration factor can be obtained by performing linear regression on this plot to obtain the y-axis intercept.

After performing linear regression on the plot in Fig. 26, the y-axis intercept was found to be 2.56 ± 0.01. This is therefore the zero-point r′ calibration magnitude value found for the Coldrick Observatory setup, assuming zero atmospheric extinction.

4.3 SEEING

GAUSS2DFIT was applied to all astronomical sources measured. This enabled a 2D Gaussian function to be produced for each image, from which the x- and y- FWHM values were able to be measured from. The average of these gave the seeing value for each image. If, for example 5 images were taken of a source, the quoted seeing value for the source would be the average FWHM for all 5 exposures, with an error of ± standard deviation of the values obtained.

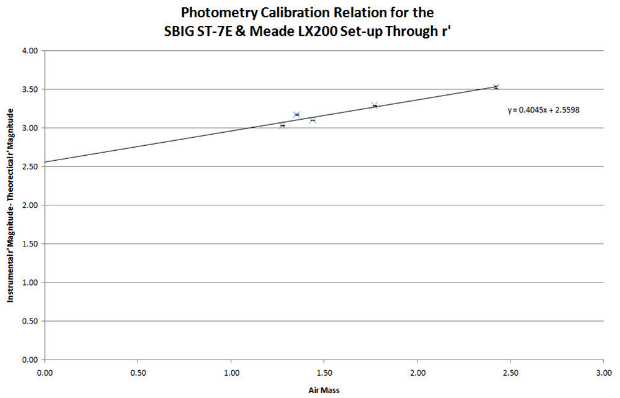

FIG. 26. Demonstrating a correlation between corrected instrumental r′ - theoretical r′ magnitude and airmass. Vertical error bars due to Poisson counting statistics. Credit to W. Foxall for this image.

The average seeing values obtained were 6.42 ± 0.77″ for the observing session on 07.03.11 and 5.02 ± 1.05″ for 24.03.11. The seeing value for HIP 31635 (r′) was not included in the value for 24.03.11, since the tracking was bad for this astronomical object. Fig. 27 demonstrates this effect as observed for HIP 31635. Seeing values for Saturn have also been omitted from this calculation, considering GAUSS2DFIT produced large seeing values for Saturn on both observing nights, due to the rings of Saturn distorting the shape and therefore the FWHM of the 2D Gaussian fitted.

The seeing values obtained for every object on both observing nights were plotted against altitude and azimuth (Fig. 28a, b) of the observed sources to determine whether there was any correlation between these values. Correlation may imply systematic bad seeing in a particular direction or altitude in Bristol on any given observing night.

Fig. 28a, b shows no immediate correlation between seeing and altitude or azimuth. In order to better visualize this relationship, the same seeing values were plotted onto a spherical surface representing the celestial sphere, binned into sections of Alt-Az 10x20° in size.

4.4 ANGULAR RESOLUTION

Fig. 30 depicts double star charts of three of the double star sources observed on 07 March 2011. The three double star objects are Mizar (HIP 65378A-C), Mintaka (HIP 25930A-C) and the brightest star in the M42 field-of-view, HIP 26235N-E. The objects have angular separations of 14.430 ″, 0.267 ″ and 0.380″, respectively [18].

Figs. 31, 32 and 33 depict 3D intensity plots from exposures taken of these objects. The plots were generated using the IDL `shade_surf`command. A rigorous method of testing whether the double stars are able to be resolved would be to fit a PSF function to either peak in these diagrams and determine whether one maximum falls about the adjacent minimum. Since the empirical data was obtained later than expected for this project, sufficient time was not available to perform analysis in this depth.

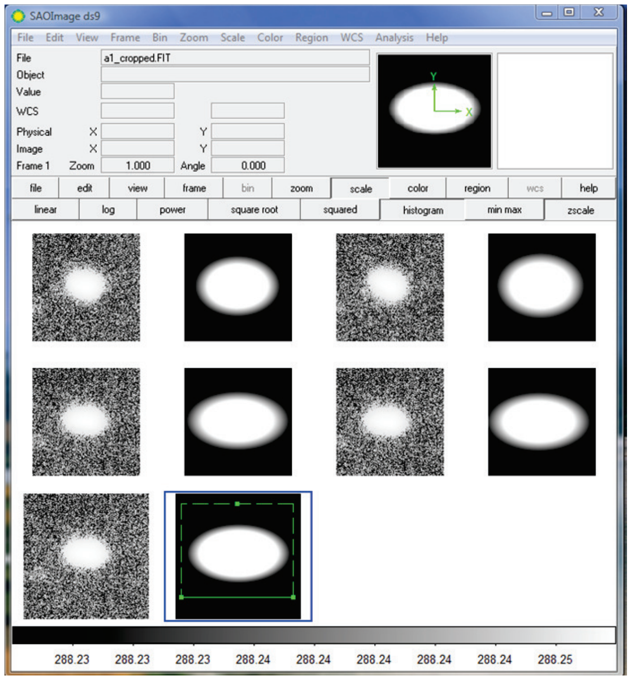

FIG. 27. Subsequent 60s exposures taken of HIP 31635. The tracking conditions were bad when these exposures were taken, and as such the PSF generated by the source increased with subsequent exposures as the star began to 'streak' further across the CCD FOV.

It can, however be visually deduced from Figs. 31, 32 and 33 which double stars were able to be resolved using the Coldrick Observatory setup. Firstly, Fig. 31 demonstrates that, despite the poor focussing of the telescope, the double star system was easily able to be resolved. Fig. 32 shows a secondary peak which is just visible next to the primary peak, suggesting this image is near the resolution limit of the telescope given the seeing conditions of the night. Fig. 33 shows that the secondary peak of the brightest star in the star in the M42 field of view was not able to be visually resolved by the LX-200 telescope.

What is interesting to note is that the 0.267 ″ separation double star system was able to be resolved whereas the 0.380″ separation double star system was not. This counter-intuitive phenomenon can be explained by the seeing on the night - the mean seeing value for Mintaka was 6.497″ whereas for the M42 double-star system it was measured as 6.896″.

This therefore conclusively proves that for worse seeing conditions, the Coldrick Observatory LX-200 telescope is less sensitive to double-star measurements. The theoretical angular resolution limit of 0.62 ″ for the device, as introduced in section 2.1.4. was not able to be obtained, due to the seeing conditions on the night.

4.5 VARIABLE SOURCES

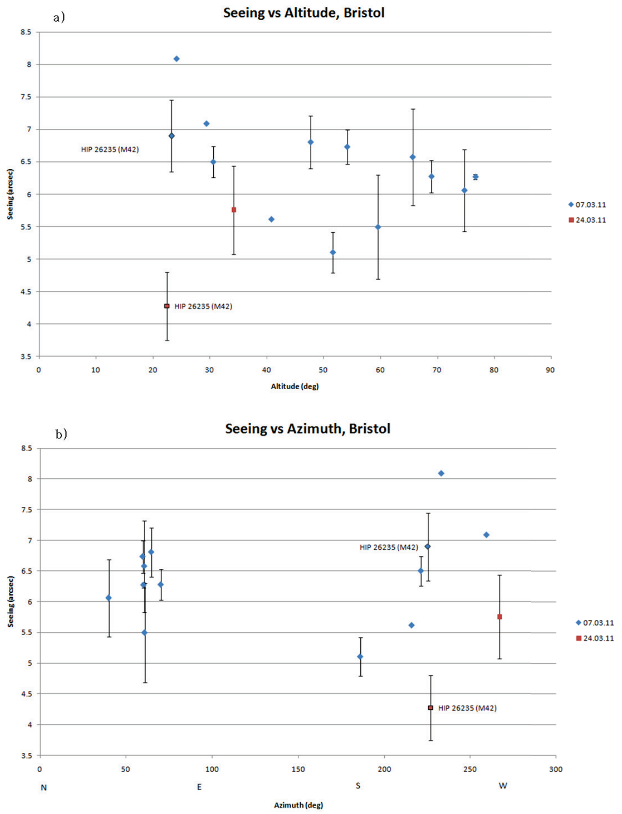

FIG. 28. Seeing values measured from the Coldrick Observatory vs altitude and azimuth of the observed objects. It is worth noting that the seeing value for HIP 26235 (M42) as measured on 07.03.11 is higher than that measured for the same object on 24.03.11. As the focusing was better on 24.03.11 due to improved technique, this demonstrates that a better seeing value is able to be obtained with more accurate focusing. Vertical error bars due to standard deviation of seeing values used to calculate the mean seeing value for each source.

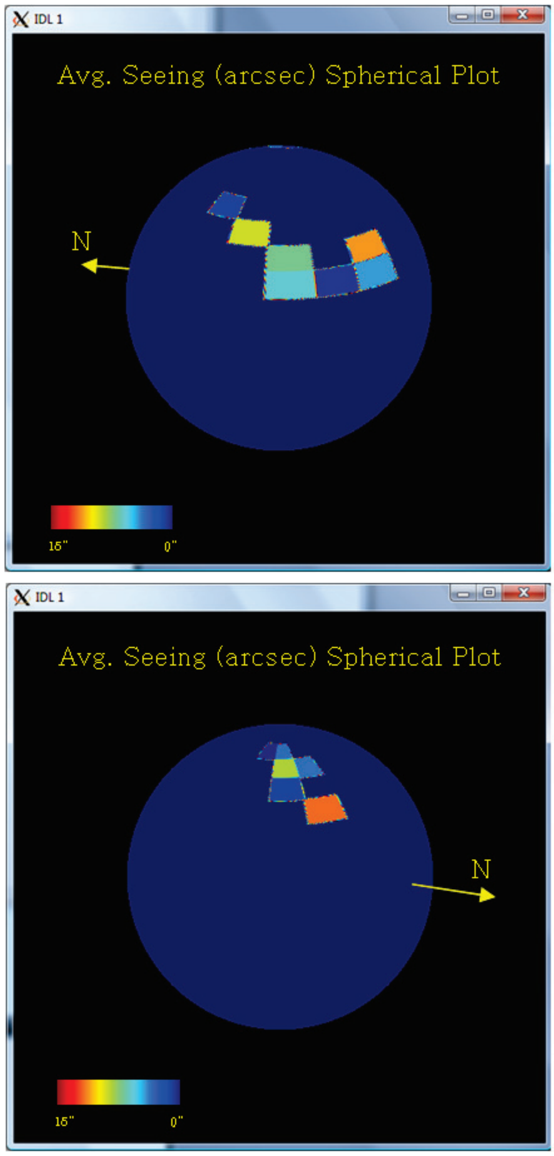

FIG. 29. A 360° spherical seeing plot highlighting the seeing values measured in different areas of the sky around Bristol. The image scale is Red-Blue: red for higher (i.e. worse) values of seeing and vice-verse for blue. Note that the blue 'background' to the sphere does not imply low seeing - rather that seeing values weren't recorded over this area. The graphs show no great correlation between the seeing values obtained and the altitude or azimuth in the sky. There is a slight hint of worsening seeing to the East, which was expected as heat vents outlets from the University of Bristol IBM supercomputer data center outlet to the East of the Coldrick Observatory dome, which would cause worsening seeing values, particularly at lower altitudes in the sky.

The M42 field of view was a repeated measurement which was taken on both 07 March 2011 and 24 March 2011 observing sessions. It was therefore possible to measure the difference in magnitudes of stellar objects within each field of frames on each date and quantify the mean amount they had changed by. A variable star could therefore also be observed to see if the difference in magnitude varied noticeably differently from that of reference, non-variable stars.

Fig. 34 depicts such a plot. HD 37042 is a suspect variable star within the M42 field-of-view, whose magnitude has varied by a greater amount than that of its neighbours. It should be noted however that the variation in magnitude observed is in fact greater than textbook measurements of this star suggest. This result is therefore not conclusive, however would be an interesting field for further research. Objects which vary by a large amount should be observed on numerous occasions of set time intervals apart to more accurately quantify the sensitivity of the Coldrick Observatory Meade LX-200 setup to variations in variable source magnitudes.

5 FURTHER RESEARCH

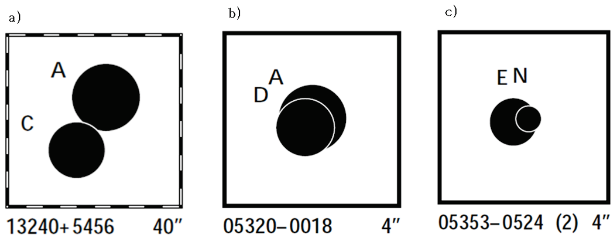

FIG. 30. Double star charts depicting double star systems of *a:* Mizar (HIP 65378A-C), *b:* Mintaka (HIP 25930A-C) and *c:* brightest star in the M42 field-of-view, HIP 26235N-E. The objects have angular separations of 14.430 ″, 0.267 ″ and 0.380″, respectively [18].

Many of the results obtained throughout this investigation very much lay the footwork for further future research to be carried out. Now that the behaviour of the SBIG ST-7E CCD device is well understood, future project students should swiftly be able to reach a stage where astronomical observations are able to be carried out far earlier into the project period. This would enable many of the results presented in this report to be investigated further. A number of possible areas for future research shall now be discussed.

An accurate plot of instrumental r′ magnitude vs. airmass would be an excellent asset, since it would enable an accurate coefficient of extinction, κ to be determined for the device. When combined with the zero-point calibration result presented in this report, the Coldrick Observatory will be able to be used as an excellent scientific tool for photometric calibration of the night sky.

The spherical seeing plots presented in this report are a good start to begin to quantify the seeing conditions in the Bristol night sky, however there are many more readings which could be taken to improve the scope and accuracy of this plot. In particular a further investigation into whether the seeing is worse to the East of the Coldrick Observatory dome due to the IBM supercomputer heat vents would be an interesting topic of investigation.

The angular resolution results presented here are somewhat primitive and considerably more research could be performed into this field. PSF overplots to accurately determine whether astronomical sources can be resolved would be a useful tool. An investigation into the seeing conditions vs angular resolution capabilities of the telescope would be beneficial to enable this relationship to be more accurately quantified.

Finally, the sensitivity of the Coldrick Observatory Meade LX-200 setup can be easily investigated by choosing a suitable variable star with a reasonably short period and performing regular observations of this star at hourly intervals or on separate observing nights. The variability sensitivity results presented here in particular are very speculatory, so of all the topics of further research this is one in which significant ground could be achieved.

The author will now present some advice to future project students to aid data collection for future research:

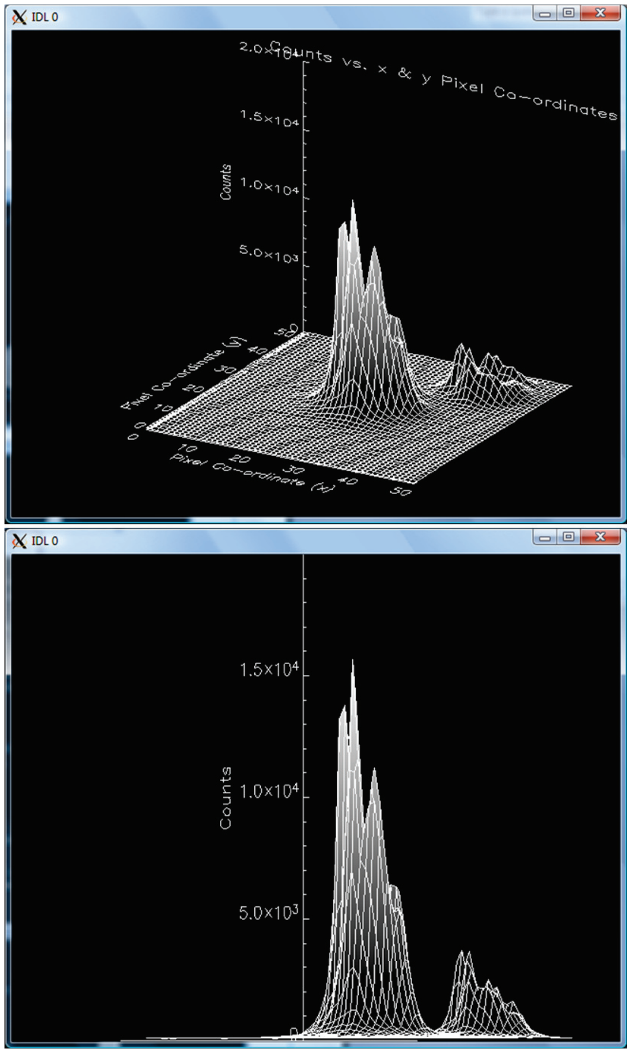

FIG. 31. `Shade_surf` plot highlighting the intensity profile of the double-star system, Mizar (HIP 65378A-C, Sep: 14.430 ″). The jagged edges surrounding each star are a result of bad focusing whilst viewing this object.

Gain plenty of practice with the Meade LX-200 device in daylight hours to maximize time efficiency on observing nights. Ensure that the telescope is able to be put into focus accurately using the CCDOps software. Centering objects in the telescope FOV is challenging due to the slow data transfer rate onto the laptop hardware; this is a skill that must be practiced and developed. Alignment of finder scope and centre of telescope FOV is absolutely mandatory to ensure accuracy on observing nights. 2-star alignment provides the best tracking, however alignment calibration objects must be a large angular distance apart to ensure the accuracy of this process. The ”offset” RA/Dec technique is very useful in helping to find faint sources and is highly recommended.

With regards to suitable target objects to observe on a given night, observers should choose one object which varies

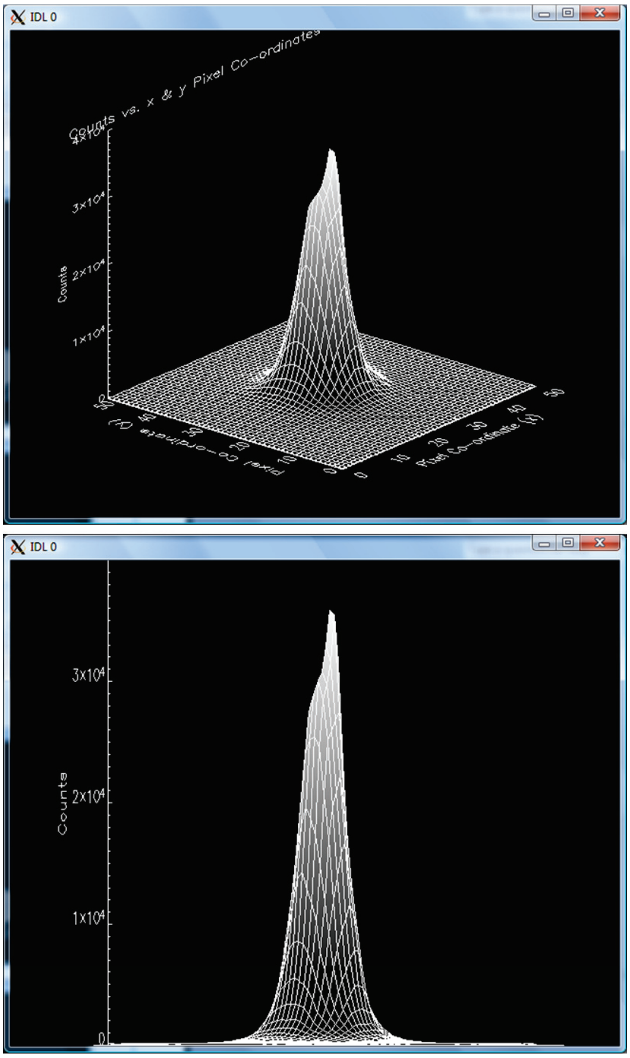

FIG. 32. `Shade_surf` plot highlighting the intensity profile of the double-star system, Mintaka (HIP 25930A-C, Sep: 0.267 $''$) The secondary peak is just able to be visually resolved.

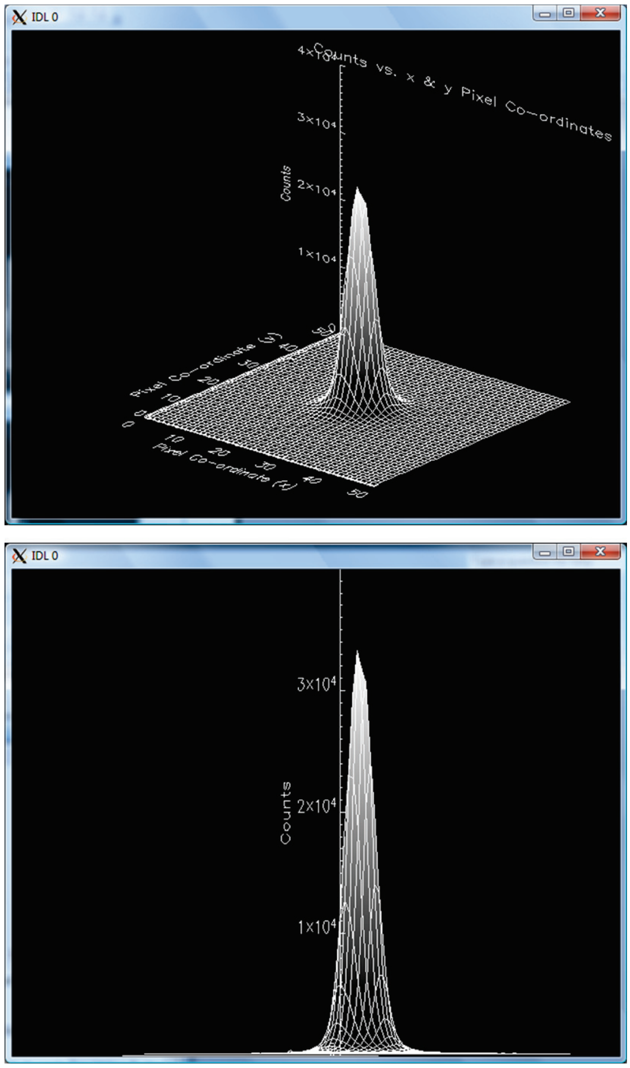

FIG. 33. `Shade_surf` plot highlighting the intensity profile of the M42 double-star system, HIP 26235N-E (Sep: 0.380 $''$). The secondary peak is not convincingly able to be visually resolved. This demonstrates that, despite having a wider angular separation than the double star system in Fig. 32, the worse seeing conditions measured about this object prevented it from being adequately resolved by the Coldrick Observatory LX-200 setup.

through a lot of airmass and observe it at regular intervals throughout the night. A variety objects should be chosen which vary dramatically in altitude and azimuth to ensure plenty of the sky is able to be covered. Observing plans often change throughout an observation session and so an observer must be fluid - be proficient with software such as Stellarium to help you choose alternative stellar objects if a given observing plan is not able to be followed.

All raw data and IDL scripts from the 2010/2011 project will be made available to future project students. This data will be stored in the home directory of the University of Bristol Starlink computers,under `/auto/project2/telescope_data/` .

6 CONCLUSION

The behaviour of the Coldrick Observatory SBIG ST-7E CCD device is now well understood. The device is sensitive to light leakage, and as such background illumination should be kept to a minimum when in use. The KAF-0401E CCD was found to be linear with dark current and photons up until $\sim$ 40,000 ADU counts. The CCD introduces progressively more noise with an increase in temperature, and so an operating temperature of -5° was chosen for both calibration and observing sessions.

The Coldrick Observatory SBIG ST-7E CCD device has been found to contain $\sim$ 10% bad pixels and $\sim$ 30% warm pixels and $\sim$ 10% cool pixels. IDL procedures were written to generate masks to identify these pixels and a routine enti-

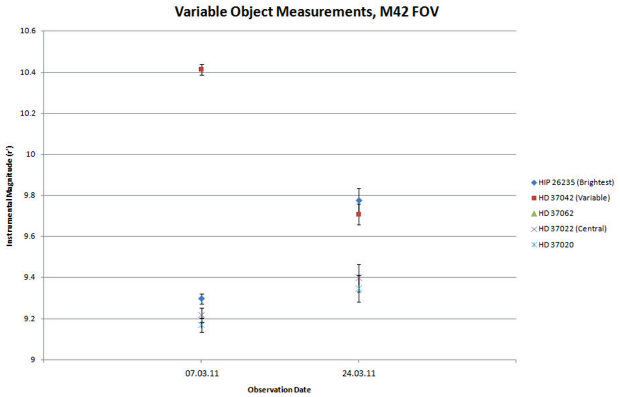

FIG. 34. Variation in magnitude of objects which were measured on both 07 March 2011 and 24 March 2011. HD37024, a suspected variable star in the M42 FOV varies by a greater amount between exposures than other, non-variable sources. This suggests the Coldrick Observatory Meade LX-200 setup may be sensitive to variations in variable star magnitudes.

tled `fixbadpixel.pro` was written to fix the anomalous bad pixel values. When performing aperture photometry, the `fixbadpixel.pro` routine is mandatory for faint sources, however only hot pixels need to be fixed.

Master bias, scalable master dark and normalized flat-field frames were able to be generated, enabling a procedure entitled `data_reduction.pro` to be written to fully reduce raw astronomical data and remove all quantifiable sources of noise.

Accurate r′ magnitude calibrations are able to be performed, with a zero-point calibration factor of 3.03 ± 0.16 before extinction has been taken into account. The zero-point calibration factor is estimated to be 2.56 ± 0.01 with zero airmass present. An accurate value for the extinction coefficient, κ was not able to be obtained.

The lowest visual magnitude star the Coldrick Observatory able to measured through a r′ filter without saturating was found to be 0.87 V_{mag}, or 0.32 r'_{mag}.

No significant correlation could be made between the seeing in Bristol and altitude or azimuth, although results suggest the seeing may be worse to the East of the Coldrick Observatory dome, where supercomputer heat outlets are situated.

Is is possible to resolve objects with as low as 0.267″ separation in seeing conditions of 6.497″. The theoretical resolution limit, 0.62″ was unable to be achieved due to the seeing conditions on both observing nights.

Results tentatively suggest the Coldrick Observatory setup may be sensitive to variable star magnitude fluctuations, however this is a topic of research which requires further investigation.

The author thoroughly enjoyed taking part in this project. The topic area was very broad and therefore a steep learning curve had to be overcome; this process was nevertheless very enjoyable and satisfying. The project was engaging throughout and has provided an insight into the world of professional astronomy. The results obtained from this investigation have developed considerably from those presented in the 2009/10 project reports and provide a stepping stone to enable a vast scope of further research to take place.

[1] Meade Instruments Corporation *Instruction Manual: 7” LX200 Maksutov-Cassegrain Telescope; 8”, 10”, and 12” LX200 Schmidt-Cassegrain Telescopes*; California, 1-64.
[2] Golding, M. *Commissioning the Optical Telescope: Seeing*; University of Bristol, 2010, 1-31.
[3] Flynn, J. *Commissioning of the Bristol University Optical Telescope: Photometry*; University of Bristol, 2010, 1-26.
[4] Huyton, P. *Calibration of the Department’s Optical Telescope with Photometry*; University of Bristol, 2010, 1-44.
[5] Norton, A. J. *Observing the Universe*; Cambridge University Press: Cambridge, 2004, 23-34.
[6] Maughan, B. *Astronomical Techniques lecture course: Handout*; University of Bristol, 2009, 25.
[7] Santa Barbara Imaging Group *ST-7 Information*; [Online], Available: http://www.sbig.com/sbwhtmls/st7.htm [10 May 2011].
[8] Santa Barbara Imaging Group *Operating Manual; CCD Camera Models ST-7E, ST-8E, ST-9E, ST-10E and ST-1001Es*; California, 2001, 1-61.
[9] Chromey, F. R. *To Measure the Sky*; Cambridge University Press: Cambridge, 2010, 243-254.
[10] Santa Barbara Imaging Group *Users Guide: CCDOps Version 5*; California, 2003, 1-123.
[11] Eastman Kodak Company - Microelectronics Technology Division *Performance Specification; KAF-0401E 768x512 Pixel Full-Frame CCD Image Sensor*; New York, 1998, 1-14.
[12] ANDOR Technology *CCD Blooming and Anti-Blooming*; [Online], Available: http://www.andor.com/learning/digital_cameras/?docid=395 [19 Nov 2010].
[13] Fukugita et al. The Sloan Digital Sky Survey Photometric System *The Astronomical Journal* **1996**, *3,4*, 1748-1756.
[14] ESA *The Hipparcos and Tycho Catalogues*, 1997, ESA SP-1200.
[15] SDSS *SDSS Photometric Equations*; [Online], Available: http://www.sdss.org/dr4/algorithms/sdssUBVRITransform.html [01 May 2011].
[16] Bushberg, J. T., et al. *The Essential Physics of Medical Imaging, 2nd Edition*; Lippincott Williams & Wilkins, Philadelphia, 2006, 280.
[17] Time and Date AS *Sunrise and Sunset for U.K. England Bristol December 2010*; [Online], Available: http://www.timeanddate.com/worldclock/astronomy.html?n=299&month=12&year=2010&obj=sun&afl=-11&day=1 [10 May 2011].
[18] ESA *The Hipparcos and Tycho Catalogues, Volume 10: Double and Multiple Systems Annex + Solar System Objects*, 1997, ESA SP-1200.

This document was written in LaTeX.

APPENDIX

A Related Colloquia/Seminars Attended

All Colloquia/Seminars venues in H.H. Wills Physics Laboratory building.

11 Oct '10: *"CMOS Monolithis Active PixelSensors (MAPS) for Scientific Applications"*
Colloqium
Dr. Renato Turchetta, Rutherford Appleton Laboratory

03 Nov '10: *"Composition and Structure of the Outer Milky Way"*
Seminar
Lee Summers, Exeter University

17 Nov '10: *"TOPCAT and Friends"*
Seminar
Mark Taylor, University of Bristol

06 Dec '10: *"Transiting Exoplanets: from Hot Jupiters to Super-Earths"*
Colloqium
Professor Ignas Snellen, University of Leiden

B IDL: Generate Median Array

```
; Generate Median Array
; Author:  B. Maughan, 2010

; This example uses 9 arrays, it can in principle be used for any number of
arrays the user wishes
; Input arrays:  "a1-9"
; Output arrays:  "a_median"
; "data" is a temporary storage array used to store a specific pixel value
from each image before the median value is chosen.
; Read input FITS files from directory and filename chosen by user.  "~"
designates user's home directory on University of Bristol Aquila system.
; "header1-9" reads in the FITS headers from the file being read in,
containing information about the FITS file itself.  It is not always madatory
to read this in, but it good practice e.g.  if the exposure length or date is
needed to be read in later on.

a1=readfits('~/array1.FIT', header1)
a2=readfits('~/array2.FIT', header2)
a3=readfits('~/array3.FIT', header3)
a4=readfits('~/array4.FIT', header4)
a5=readfits('~/array5.FIT', header5)
```

```
a6=readfits('~/array6.FIT', header6)
a7=readfits('~/array7.FIT', header7)
a8=readfits('~/array8.FIT', header8)
a9=readfits('~/array9.FIT', header9)
s=size(a1)
sx=s[1]-1
sy=s[2]-1
a_median=a1
for i=0,sx do begin &$
for j=0,sy do begin &$
data=[a1[i,j], a2[i,j], a3[i,j], a4[i,j], a5[i,j], a6[i,j], a7[i,j], a8[i,j],
a9[i,j]] &$
a_median[i,j]=median(data) &$
endfor &$
endfor
```

C IDL: fixbadpixel.pro, Flow Diagram

See figure 1 overleaf.

D IDL: fixbadpixel.pro

```
; fixbadpixel.pro, v1.1.1.
; Author:  R. Painter, BSc Project Student '10/'11, 30.03.11
; Calling sequence:  result=fixbadpixel(data, mask)

; Input mask supplied by the user must consist of pixel values of 1 and 0 only
and must be of the same dimensions as the input data array.

FUNCTION fixbadpixel,data,mask

  data=data
mask=mask

  size_data=size(data)
size_mask=size(mask[where(mask eq 0)])

  data=float(data)
data[where(mask eq 0)]=!values.f_nan

  width=size_data[1]
height=size_data[2]

  rows=long(size_mask[3])
bad=long(size_mask[3])
```

```
  a=long(0)

  ; Add single pixel 'border' around data:

  databorder=fltarr(width+2,height+2)

  For i=0,width-1 do begin &$
For j=0,height-1 do begin &$
databorder[i+1,j+1]=data[i,j] &$

  Endfor &$
Endfor

  ; Let border values equal NaN

  databorder[0:width+1,0]=!values.f_nan
databorder[0:width+1,height+1]=!values.f_nan
databorder[0,0:height+1]=!values.f_nan
databorder[width+1,0:height+1]=!values.f_nan

  ; Get bad x & y coordinates (add 1 when translating to info due to extra
border dimension)

  info=lonarr(3,rows)

  For i=0,width-1 do begin &$
For j=0,height-1 do begin &$
value = mask[i,j] &$

  If value eq 0 then begin &$
info(0,a) = i+1 &$
info(1,a) = j+1 &$
a=a+1 &$
Endif &$

  Endfor &$
Endfor

  ; While bad pixels remain

  While (bad ne 0) do begin &$

  ; Calculate number of free pixels ('availability') around bad pixels (CW
from top-left of bad pixel)

  For i=0L,rows-1 do begin &$

  If (info[2,i] ne -1) then begin &$
x=info[0,i] &$
y=info[1,i] &$
free=0 &$
```

```
  If (databorder[x-1,y-1] gt 0) then begin &$
free=free+1 &$
Endif &$
If (databorder[x,y-1] gt 0) then begin &$
free=free+1 &$
Endif &$
If (databorder[x+1,y-1] gt 0) then begin &$
free=free+1 &$
Endif &$
If (databorder[x+1,y] gt 0) then begin &$
free=free+1 &$
Endif &$
If (databorder[x+1,y+1] gt 0) then begin &$
free=free+1 &$
Endif &$
If (databorder[x,y+1] gt 0) then begin &$
free=free+1 &$
Endif &$
If (databorder[x-1,y+1] gt 0) then begin &$
free=free+1 &$
Endif &$
If (databorder[x-1,y] gt 0) then begin &$
free=free+1 &$
Endif &$

  info[2,i]=free &$

  Endif &$

  Endfor &$

  ; Sort info by 3rd column (availability), decreasing

  order=reverse(sort(info[2,*])) &$
info=info(*,order) &$

  ; For pixels with best availability, let bad pixel value equal mean of
surrounding nonzero pixels

  max=max(info[2,*]) &$

  For i=0L,rows-1 do begin &$

  If (max ne -1) then begin &$
While (info[2,i] eq max) do begin &$

  x=info[0,i] &$
y=info[1,i] &$
a=[databorder[x-1,y-1],databorder[x,y-1],databorder[x+1,y-1],databorder[x+1,y]
&$
```

```
databorder[x+1,y+1],databorder[x,y+1],databorder[x-1,y+1],databorder[x-1,y]]
&$
databorder[x,y]=mean(a, /nan) &$
info[2,i]=-1 &$
bad=bad-1 &$

  Endwhile &$
Endif &$
Endfor &$

  Endwhile

  ; Transfer data from 'result' array back to original array:

  For i=0,width-1 do begin &$
For j=0,height-1 do begin &$
data[i,j] = databorder[i+1,j+1] &$

  Endfor &$
Endfor

  return,data
end
```

E Magnitude Conversion Equations: $B_{mag}/(B\text{-}V)_{mag} \rightarrow r'_{mag}$

$$r = V - 0.42 * (B - V) + 0.11 \qquad (\pm 0.03) \tag{1}$$

$$g = V + 0.60 * (B - V) - 0.12 \qquad (\pm 0.02) \tag{2}$$

$$R_c = r - 0.1837 * (g - r) - 0.0971 \qquad (\pm 0.0106) \tag{3}$$

$$R_c = r - 0.2936 * (r - i) - 0.1439 \qquad (\pm 0.0072) \tag{4}$$

$$I_c = r - 1.2444 * (r - i) - 0.3820 \qquad (\pm 0.0078) \tag{5}$$

$$r' - i' = 1.070(\pm 0.009) * (R_c - I_c) - 0.228 \tag{6}$$

$$r' = r - [0.035 * ([r' - i'] - 0.21)] \tag{7}$$

F IDL: data_reduction.pro

```
; data_reduction.pro, v1.0.
; Author:  R. Painter, BSc Project Student '10/'11, 30.03.11.
; Calling sequence:  result=data_reduction(data,exposure,mbias,mdark,mflat,mask)

; Input exposure must be in seconds
; The exposure time in seconds of a SBIG ST-7E FITS file is able to be read in
from its header using the following code:  exposure=fxpar(header,'date-obs')

; Steps:  Raw -> -master bias -> -scalable master dark -> /normalized master
flat -> pixel fix w/ appropriate mask

FUNCTION data_reduction,data,exposure,mbias,mdark,mflat,mask

  data_red=data
exposure_min=exposure/60
mbias=mbias
mdark=mdark
mflat=mflat
mask=mask

  ; subtract mbias & scalable mdark, ensuring non-zero during subraction phase

  data_red=data_red+100000

  data_red=data_red-mbias

  data_red=data_red-[mdark/(30/exposure_min)]

  data_red=data_red-100000

  ; zero array, if negative values remain

  min=min(data_red)

  if min lt 0 then begin &$
data_red=data_red-min &$
endif

  ; divide by normalized mflat

  data_red=data_red/mflat

  ; fix bad pixels, using input mask

  data_red=fixbadpixel(data_red,mask)

  ; restore negative values, if array previously zeroed
```

```
  if min lt 0 then begin &$
data_red=data_red+min &$
endif

  return,data_red
end
```

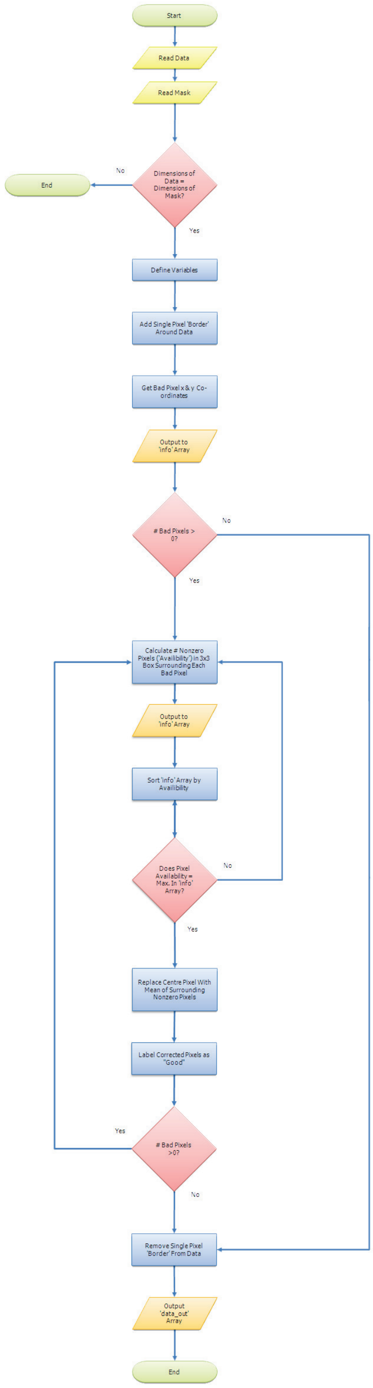

Figure 1: Flow diagram depicting the programming logic behind the `fixbadpixel.pro` procedure.

Date Observed	Time	Object	Type	Name	HIP	Vmag mag	B-V mag	r mag	**r' mag theoretical**	*r' mag instrumental*	*r' mag corrected (ADU & quantum efficiency)*	*r' mag corrected - r' mag theoretical*	***r' mag calibrated***	*Accuracy of r' mag calibrated*
07.03.11	20:00	Binary, Observing Plan #8	Double	e Gem	33202A-B	4.73	0.321	4.7052	**5.0593**	*9.2993*	*7.8328*	*2.7736*	***4.7964***	*0.2629*
07.03.11	20:30	Andromeda Galaxy	Deep-Field	M31	-	-	-							
07.03.11	20:50	-	Star	Betelgeuse	27989	0.45	1.5	-0.07	**-0.1169**	*4.5812*	*3.1147*	*3.2316*	***0.0782***	*0.1951*
07.03.11	21:00	Orion's Belt, R	Double	Mintaka	25930A-C	2.25	-0.175	2.4335	**2.6357**	*7.2725*	*5.8060*	*3.1703*	***2.7696***	*0.1339*
07.03.11	21:10	Orion Nebula	Deep-Field	M42	26235N-E	-	-			*9.2972*				
07.03.11	21:10	Orion Nebula	Deep-Field	M42	-					*10.4141*				
07.03.11	21:45	Orion's Belt, M	Star	Alnilam	26311	1.69	-0.184	1.8773	**2.0381**	*6.8371*	*5.3706*	*3.3324*	***2.3341***	*0.2960*
07.03.11	21:59	-	Star	Aldebaran	21421	0.87	1.538	0.334	**0.3160**	*4.9651*	*3.4986*	*3.1826*	***0.4621***	*0.1461*
07.03.11	22:15	Plough #1	Star	Alkaid	67301	1.85	-0.099	2.0016	**2.1686**	*6.7352*	*5.2687*	*3.1001*	***2.2323***	*0.0637*
07.03.11	22:25	Plough #2	Double	Mizar	65378A-C	2.23	0.057	2.3161	**2.5009**	*6.8376*	*5.3711*	*2.8702*	***2.3346***	*0.1663*
07.03.11	22:30	Plough #3	Star	Alioth	62956	1.76	-0.022	1.8792	**2.0343**	*6.5334*	*5.0669*	*3.0326*	***2.0305***	*0.0038*
07.03.11	22:35	Plough #4	Star	Megrez	59774	3.32	0.077	3.3977	**3.6628**	*8.0440*	*6.5775*	*2.9147*	***3.5411***	*0.1217*
07.03.11	22:40	Plough #5	Star	Phad	58001	2.41	0.044	2.5015	**2.7007**	*7.1755*	*5.7090*	*3.0083*	***2.6726***	*0.0281*
07.03.11	22:45	Plough #6	Star	Merak	53910	2.34	0.033	2.4361	**2.6309**	*7.0951*	*5.6286*	*2.9978*	***2.5922***	*0.0387*
07.03.11	22:50	Plough #7	Double	Dubhe	54061A-B	1.81	1.061	1.4744	**1.5593**	*6.1104*	*4.6439*	*3.0846*	***1.6074***	*0.0481*
07.03.11	23:00	Saturn	Solar System	Saturn	-	0.86	-							
24.03.11	20:00	Pleiades Cluster	Star	Maia	17573	3.87	-0.063	4.0065	**4.3223**	*8.8831*	*7.4166*	*3.0943*	***4.3802***	*0.0579*
24.03.11	20:20	Orion Nebula	Deep-Field	M42	26235N-E	4.98	-0.097	5.1307	**5.5321**	*9.7762*	*8.3097*	*2.7776*	***5.2732***	*0.2588*
24.03.11	21:10	Orion Nebula	Deep-Field	M42	-					*9.7086*				
24.03.11	23:10	r', Observing Plan #2	Star	LHS 1858	31635	9.63	1.48	9.1184	**9.7604**	*14.2029*	*12.7364*	*2.9760*	***9.7000***	*0.0605*
24.03.11	23:40	Saturn	Solar System	Saturn	-	0.86	-							
24.03.11	23:59	Variable #1 FOV	Stars	FOV	-	-	-							
										Average mag calibration factor:		*3.0364*		
										-> Due to variety of factors; e.g. Extinction coefficient, poor photometric conditions etc.				
										-> The important thing is that the factor is ≈ constant (±10%) for every star measured.				

Figure 2: Summary table of all astronomical objects observed on both observing nights: 07.03.11 & 24.03.11. Empirical and textbook r′ values have been included. The difference between these 2 sets of values for each object had a small standard deviation and an average magnitude calibration factor of 3.0364 r'_{mag}.